МІНІСТЕРСТВО ОСВІТИ І НАУКИ УКРАЇНИ
ДВНЗ «УЖГОРОДСЬКИЙ НАЦІОНАЛЬНИЙ УНІВЕРСИТЕТ»

НАУКОВИЙ ВІСНИК
УЖГОРОДСЬКОГО УНІВЕРСИТЕТУ

СЕРІЯ
«ФІЗИКА»

Науковий журнал

Випуск 48
2020

УЖГОРОД
2020

ISSN 2415-8038

Засновником журналу Науковий вісник Ужгородського університету. Серія «Фізика» є
ДВНЗ «Ужгородський національний університет», фізичний факультет
та Закарпатське фізичне товариство

Рекомендовано до друку та поширення
через мережу Інтернет Вченою Радою
ДВНЗ «Ужгородський національний університет»
(протокол № 9 від 22 грудня 2020 р.)

Свідоцтво про державну реєстрацію
друкованого засобу масової інформації
Серія КВ № 7972 від 09.11.2003 р.

Збірник входить до переліку фахових видань України
Категорія: Б. Науки: фізико-математичні. Спеціальності: 104 – Фізика та астрономія,
105 – Прикладна фізика та наноматеріали
(Наказ Наказ Міністерства освіти і науки України від 11.07.2019 р. № 975)

Збірник представлено у міжнародних наукометричних базах даних,
репозиторіях та пошукових системах: Google Scholar, BASE, НБУ ім. В.І. Вернадського,
Crossref, OpenAIRE, WorldCat

Адреса редакції:
ДВНЗ «Ужгородський національний університет»
88000, вул. Волошина, 54, м. Ужгород
Закарпатська область, Україна
тел/факс: (03122) 3-20-24
E-mail: info@physics.uz.ua
www: https://physics.uz.ua/uk

MINISTRY OF EDUCATION AND SCIENCE
OF UKRAINE UZHHOROD NATIONAL UNIVERSITY

SCIENTIFIC HERALD
OF UZHHOROD UNIVERSITY

SERIES
“PHYSICS”

Scientific Journal

Issue 48
2020

UZHHOROD
2020

ISSN 2415-8038

The journal Scientific Herald of Uzhhorod University. Series “Physics” is founded
by Faculty of Physics, Uzhhorod National University
and Transcarpathian Physical Society

Recommended for printing and distribution
via the Internet by the Academic Council
of Uzhhorod National University
(Minutes No. 9 of December 22, 2020)

Certificate of state registration
of the print media
Series KV No. 7972 of 09.11.2003

The collection is included in the list of professional publications of Ukraine
Category: B. Branch of Sciences: Physics and Mathematics. Specialty: 104 – Physics and Astronomy,
105 – Applied Physics and Nanomaterials (Order of the Ministry of Education and Science of Ukraine
of 11.07.2019 No. 975)

The collection is presented international scientometric databases, repositories and scientific systems: Google Scholar, BASE, VNLU, Crossref, OpenAIRE, WorldCat

The address of Editorial Board:
Uzhhorod National University
88000, 54 Voloshyn Str., Uzhhorod
Transcarpathian region, Ukraine
Tel./fax: (03122) 3-20-24
E-mail: info@physics.uz.ua
www: https://physics.uz.ua/en

НАУКОВИЙ ВІСНИК УЖГОРОДСЬКОГО УНІВЕРСИТЕТУ. СЕРІЯ «ФІЗИКА»
ВИПУСК 48

ЗМІСТ

SCIENTIFIC HERALD OF UZHHOROD
UNIVERSITY. SERIES "PHYSICS"
ISSUE 48

CONTENTS

Scientific Herald of Uzhhorod University
Series "Physics"

Journal homepage: https://physics.uz.ua/en
Issue 48, 38-49
Received: 20.07.2020. Revised: 25.10.2020. Accepted: 10.12.2020

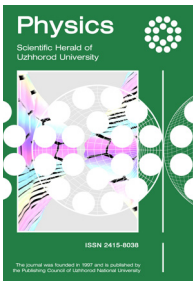

УДК 539.173+539.173.8+5393.1.6
PACS 24.75.+1, 25.85.-w, 25.85.Ec, 25.85. Ca
DOI: 10.24144/2415-8038.2020.48.38-49

Simulation the Yields of Actinide Nuclei Photofission Products as Sources of Delayed Gamma Radiation for the Needs of Analyzing their Isotopic Composition

I.V. Pylypchynets*, E.V. Oleynikov, O.O. Parlag

Instutute of Electron Physics, National Academy of Sciences of Ukraine,
88017, 21 Universitetska Str., Uzhhorod, Ukraine

Abstract

Purpose. One of the most important tasks of the nuclear industry is to control the non-proliferation of fissile nuclear materials (for example ^{232}Th, ^{235}U, ^{238}U, ^{239}Pu) at all stages of their use (movement, storage, etc.). To successfully solve this problem, reliable information about their isotopic composition is required. The present study aims to simulate the yields of pairs of photofission products of ^{232}Th, ^{235}U, ^{238}U, ^{239}Pu nuclei, the delayed gamma radiation of which can be used for nondestructive isotopic analysis of nuclear materials at electron accelerators.

Methods. Calculations of the mass distributions of the photofission products of ^{232}Th, ^{235}U, ^{238}U, ^{239}Pu nuclei were carried out using the GEF code. The bremsstrahlung spectrum was simulated during the interaction of electrons (E=12.5 MeV) with a tantalum converter (1 mm) using a GEANT4 10.7.

Results. Simulations of mass distributions of photofission products of ^{232}Th, ^{235}U, ^{238}U, ^{239}Pu nuclei have been carried out. The yields ratios for product pairs (Y_{88}/Y_{135}, Y_{92}/Y_{135}, Y_{92}/Y_{138}, Y_{87}/Y_{138}, Y_{88}/Y_{138}, Y_{89}/Y_{138}, Y_{87}/Y_{142}, Y_{88}/Y_{142}, Y_{89}/Y_{142}) are calculated for the indicated cores. Estimates of the difference between the numerical values of the ratio of yields of pairs of fragments for pairs of nuclei ^{232}Th and ^{235}U, ^{235}U and ^{238}U, ^{238}U and ^{239}Pu are made on a percentage basis. The values of the difference in the ratios of the yields of these pairs of products are – 5.0÷43.2%, 14.1÷39.3%, and 14.1÷39.3% for nuclear pairs ^{232}Th and ^{235}U, ^{235}U and ^{238}U, ^{238}U and ^{239}Pu, respectively.

Conclusions. The results of the simulation indicate the possibility of using the above pairs of fission products as sources of delayed gamma radiation when performing nondestructive isotopic analysis of nuclear materials. The results obtained can be used to optimize experiments on electron accelerators, which will improve the accuracy and reliability of the results

Keywords: nuclear materials, isotope analysis, photofission, product yields, delayed gamma radiation

Suggested Citation:
Pylypchynets IV, Oleynikov EV, Parlag OO. Simulation the yields of actinide nuclei photofission products as sources of delayed gamma radiation for the needs of analyzing their isotopic composition. *Scientific Herald of Uzhhorod University. Series "Physics"*. 2020;(48):38-49.

*Corresponding author

Introduction

One of the most important tasks of the nuclear industry is to control the non-proliferation of fissile nuclear materials (for example ^{232}Th, ^{235}U, ^{238}U, ^{239}Pu) at all stages of their use (movement, storage, etc.). To successfully solve this problem, reliable information about their isotopic composition is required. As a rule, transportation and storage of nuclear materials is carried out in hermetically sealed capsules or containers made of stainless steel [2; 3].

One of the widely used non-destructive methods for the detection and isotopic identification of unshielded and shielded fissile nuclear materials is based on the use of delayed gamma radiation from the products of their separation [4-6]. The essence of this method is to use experimentally obtained information on the ratio of the intensity of stimulated delayed gamma radiation from light and heavy products of their separation. The yields of light products-fragments significantly depend on the mass of fissile nuclei, so at the same excitation energies their mass distributions shift towards larger masses with increasing mass of fissile nucleus. At the same time, the mass distribution of heavy fragments is almost constant and does not depend significantly on the mass of the fissile nucleus.

Fission products that are potential sources of delayed gamma radiation suitable for the analysis of shielded and unshielded nuclear materials must satisfy a number of basic requirements: a) a high probability of their formation in the fission process; b) the presence of a wide set of intense gamma radiation lines with energies > 1000 MeV, free from spectrometric interference (characteristic, background gamma lines, from the products of accompanying reactions) c) with convenient half-lives for analysis. It should be noted that fission product pairs with close half-lives should be used in the analysis.

The following products-fragments meet these requirements: ^{87}Kr, ^{88}Kr, ^{88}Rb, ^{89}BRb, ^{92}Sr, ^{135}I, ^{138}Cs, ^{142}La, which were formed as a result of (n, f)-reactions induced by thermal, fast and high-energy (14 MeV) neutrons [4-6] and bremsstrahlung of electronic accelerators [7-9]. Their nuclear-physical characteristics [10] meet the above criteria. The above works [4-9] demonstrated the possibility of using them for the isotopic identification of unshielded [4-7] and shielded [8; 9] fissile nuclear materials.

The aim of the presented work is to analyze the possibility of using these nuclides-fragments (with A = 87, 88, 89, 92, 135, 138, 142) as potential sources of delayed gamma radiation, to identify 4 main fissile nuclear materials (^{232}Th, ^{235}U, ^{238}U, ^{239}Pu) when they are activated by bremsstrahlung obtained on an electronic accelerator – a microtron. Therefore, it was necessary to calculate the dependence of number values of post-neutron output of pairs of fragments (Y_{88}/Y_{135}, Y_{92}/Y_{135}, Y_{92}/Y_{138}, Y_{87}/Y_{138}, Y_{88}/Y_{138}, Y_{89}/Y_{138}, Y_{87}/Y_{142}, Y_{88}/Y_{142}, Y_{89}/Y_{142}) for the above mentioned fissile nuclei produced at the stimulation of the of photofission reaction.

Modelling Post-Neutron Outputs of Actinide Nuclear Photofission Products

In order to solve this problem, it is necessary to model post-neutron yields of photofission products of actinides ^{232}Th, ^{235}U, ^{238}U, ^{239}Pu at a fixed energy of bremsstrahlung, and to calculate the numerical values of the ratios of the pairs of fragments whose delayed gamma radiation analysis is nuclei. Delayed gamma radiation suitable for isotopic analysis of the specified nuclei.

The GEF code [11], which allows the calculation of characteristics for fissile nuclei in any type of fission (spontaneous, neutron and proton induced, photofission) and which can be used to calculate the post-neutron yields of photofission products of actinides [12; 13], was used for modelling.

The simulation is carried out for brake radiation, which is generated by electricity with energy of 12.5 MeV at a tantalum radiator with

thickness of 1 mm. The bremsstrahlung spectrum was simulated during the interaction of electrons (E=12.5 MeV) with a tantalum converter (1 mm) using a GEANT4 10.7 [14; 15], with the following input parameters: the number of events – 10^8, and for the distances: electron source – bremsstrahlung target – irradiated object, which were – 18 and 100 mm, respectively. The choice of the specified energy was due to the possibility of isotopic analysis for both unshielded and shielded fissile nuclear materials [16], i.e. the energy was lower than the thresholds of possible photonuclear reactions for potential elements from which stainless steel containers are made.

The results of the calculation of the spectrum of bremsstrahlung with an energy of 12.5 MeV are presented in Figure 1. The same figure shows the cross sections (γ, f) – reactions for ^{232}Th, ^{235}U, ^{238}U, ^{239}Pu actinide nuclei from the library of estimated nuclear data ENDF [17], which were used to calculate the average excitation energy for these fissile nuclei [12].

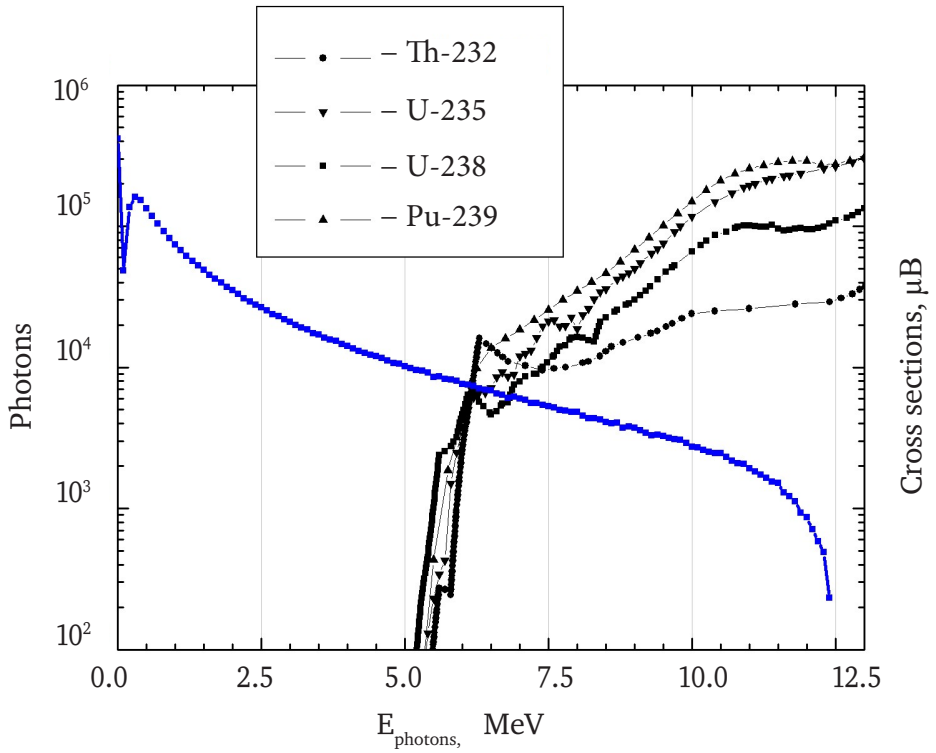

Figure 1. Braking radiation spectrum and photofission cross sections of ^{232}Th, ^{235}U, ^{238}U and ^{239}Pu

The calculated average excitation energy for the photofission of the ^{232}Th, ^{235}U, ^{238}U, ^{239}Pu nuclei at the maximum braking radiation energies of 12.5 MeV were – 8,821; 10,013; 9,744 and 9,922 MeV, respectively. The obtained values were used as input data in the GEF code simulation of post-neutron outputs of products for fissile nuclei ^{232}Th*, ^{235}U*, ^{238}U*, ^{239}Pu*. The latest version of the GEF code – 2020 / 1.1 [18] was used for calculations.

The results of the calculation of post-neutron yields of fission products are presented in the panel of Figure 2. The existing experimental data that were studied at close excitation energies are also presented here. Excitation energy values – for ^{232}Th: 8.8 MeV [19], 8.35 MeV [20]; ^{235}U: 9.7 MeV [21]; ^{238}U: MeV 9.7 [22], 9.09 MeV [23].

The results of modeling the post-neutron yields of ^{239}Pu were compared with the estimated values of the yields of the reaction products ^{238}Pu

(n_{fast}, f) [24] resulting in a similar fissile nuclei $^{239}Pu^*$, as there are no experimental data on the yields of photofission of products at close energies. The average excitation energy $<E^*>$ for the fissile nucleus $^{239}Pu^*$ in neutron fission was calculated from the average neutron energy $<E_n>$ by formula (1):

$$<E^*> = (\Delta^{238}Pu + \Delta n - \Delta^{239}Pu) + <E_n> \quad (1)$$

where Δ – excess (or defect) of the mass, the values of which were taken from [25]. The value of $<E^*>$=6.14 MeV.

The results of the calculations are consistent with the experimental data within the errors for fissile nuclei ^{235}U, ^{238}U, ^{239}Pu at close excitation energies. For ^{232}Th, there is a discrepancy between the calculated and experimental yields values [19; 20] for both light and heavy products (with maximum yields values). It should be noted that for ^{232}Th there is also a discrepancy between the existing experimental data.

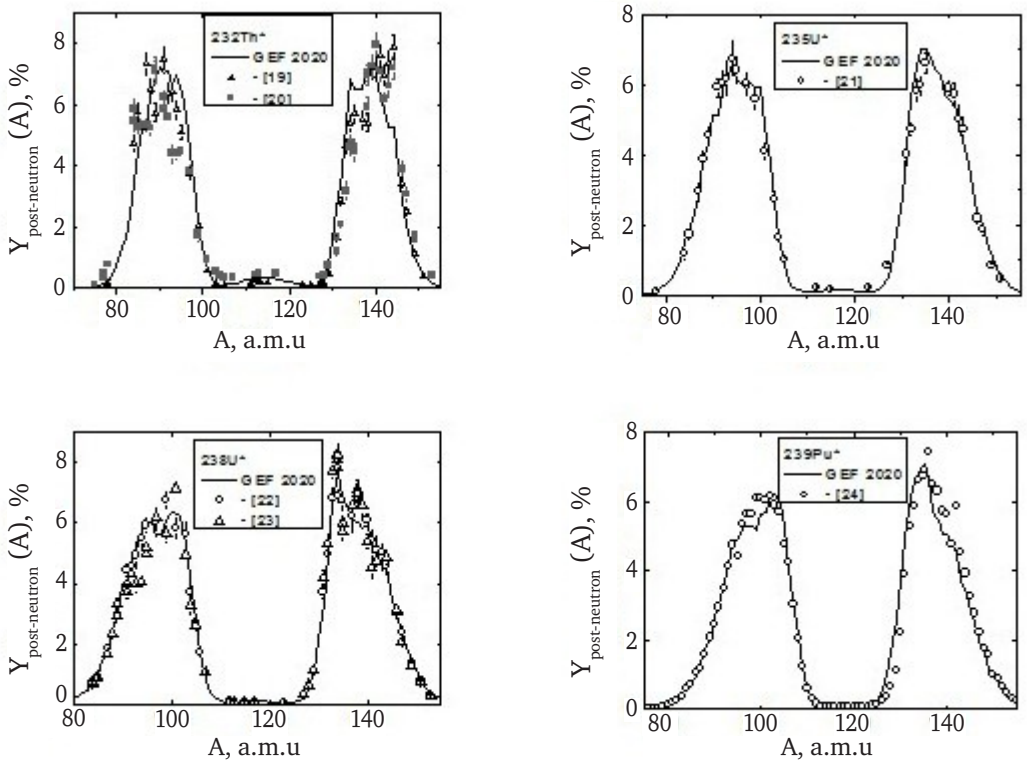

Figure 2. Post-neutron product yields for fissile ^{232}Th, ^{235}U, ^{238}U and ^{239}Pu nuclei

Figure 3 shows the dependences of post-neutron yields of photofission products of ^{232}Th, ^{235}U, ^{238}U, ^{239}Pu on product mass at the same brake radiation energy of 12.5 MeV. As can be seen from the mass distributions shown in the figure, the yields of light products shifts towards larger masses, increasing the mass of the fissile nucleus. At the same time, the mass distribution of heavy fragments remains virtually unchanged and does not depend significantly on the mass of the fissile nucleus. This indicates that the yields of light photofission products of actinide nuclei ^{232}Th, ^{235}U, ^{238}U, ^{239}Pu depend on the mass of fissile nuclei at the same stimulation energies.

The dependence of the ratios (Y_L/Y_H) of the numerical values of the yields of light (Y_L) and heavy (Y_H) products on the mass of fissile

nuclei is calculated. The calculations were performed for the following product pairs Y_{88}/Y_{135}, Y_{92}/Y_{135}, Y_{92}/Y_{138}, Y_{87}/Y_{138}, Y_{88}/Y_{138}, Y_{89}/Y_{138}, Y_{87}/Y_{142}, Y_{88}/Y_{142}, Y_{89}/Y_{142}. The fission products selected for analysis are potential sources of delayed gamma radiation suitable for isotopic analysis of shielded and unshielded nuclear materials and meet the above requirements: $Y_{87}=Y_{87Kr}$, $Y_{88}=Y_{88Kr}$, $Y_{89}=Y_{89Rb}$, $Y_{92}=Y_{92Sr}$, $Y_{135}=Y_{135I}$, $Y_{138}=Y_{138Cs}$, $Y_{142}=Y_{142La}$ [10].

The results of the calculation Y_L/Y_H are presented in panel Figure 4. As can be seen from the figure, the output ratio depends on the mass of the fissile nuclei. Here, the Y_L/Y_H yields ratios are presented, for which experimental data were used [19-24]. The obtained data are consistent with each other within the experimental errors.

Table 1 shows the numerical values of the Y_L/Y_H yields ratio for the fissile nuclei ^{232}Th, ^{235}U, ^{238}U, ^{239}Pu and the difference (percentage) in percent (%) between the numerical values of the ratio of pairs of fragments for these nuclei. The percentage difference was calculated between the pairs of nuclei ^{232}Th and ^{235}U (5.0÷43.2%), ^{235}U and ^{238}U (14.1÷39.3%), ^{238}U and ^{239}Pu (14.1÷31.4%).

Thus, the selected product pairs of photofission nuclei ^{232}Th, ^{235}U, ^{238}U, and ^{239}Pu can be used as sources of delayed gamma radiation in non-destructive isotope analysis of these actinides.

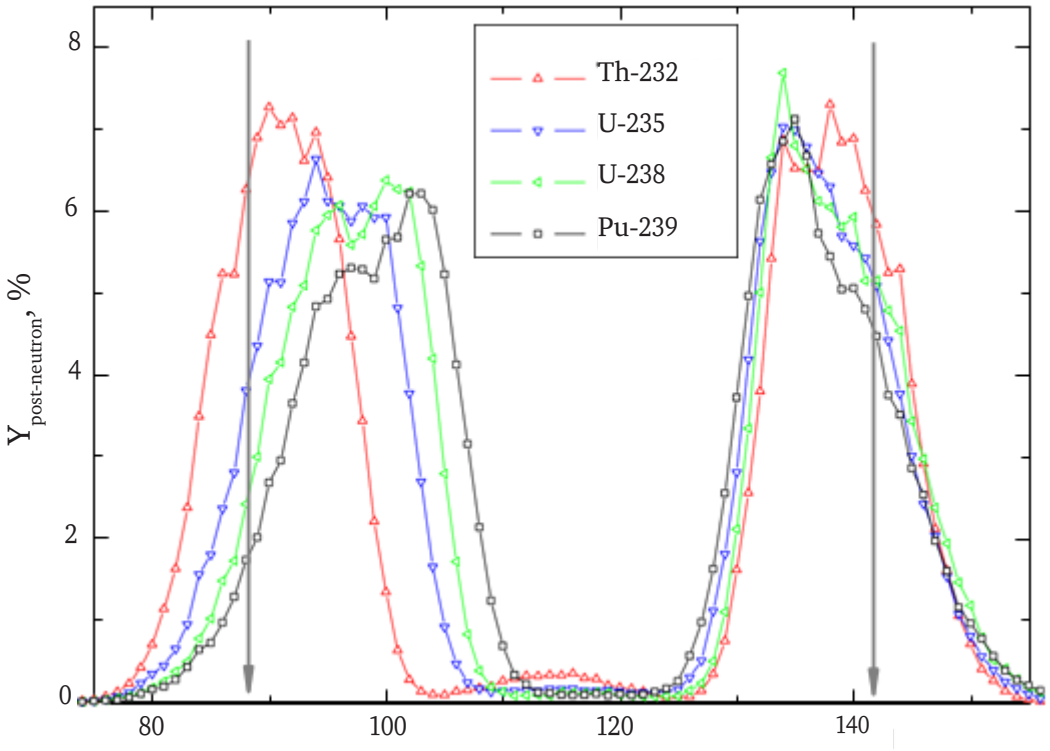

Figure 3. Dependence of post-neutron yields of fission products ^{232}Th*, ^{235}U*, ^{238}U*, and ^{239}Pu* on their mass

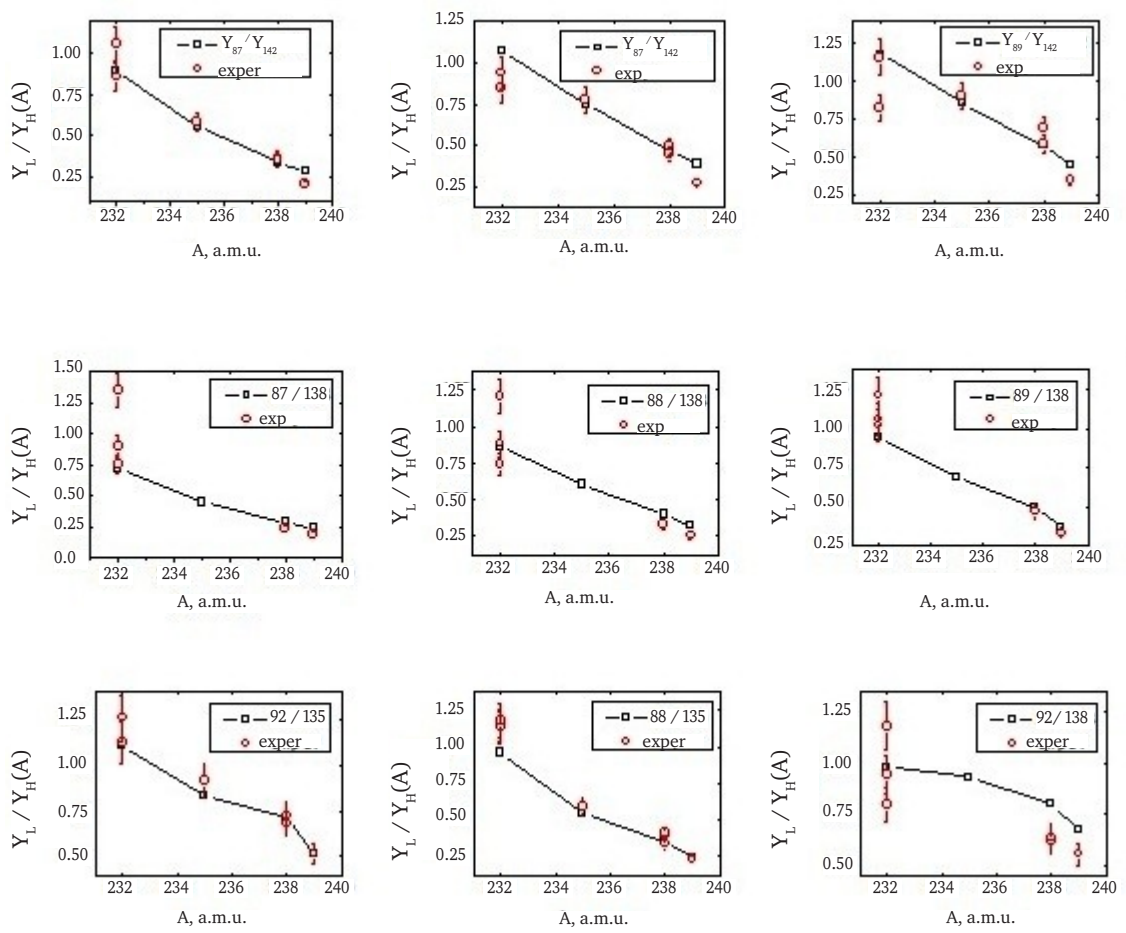

Figure 4. Dependence of the ratios of the numerical values of the yields of light and heavy products on the mass of fissile nuclei ^{232}Th, ^{235}U, ^{238}U, ^{239}Pu

Table 1. Numerical values of the Y_L/Y_H yields ratio for fissile nuclei ^{232}Th, ^{235}U, ^{238}U, ^{239}Pu, and the value of the difference in the yields ratios between adjacent pairs of nuclei

Y_L/Y_H	^{232}Th	%	^{235}U	%	^{238}U	%	^{239}Pu
Y_{88}/Y_{135}	0,95918	43.2	0,54439	34.7	0,35532	31.4	0,24371
Y_{92}/Y_{135}	1,1013	24.0	0,8372	15.2	0,70991	27.8	0,51245
Y_{92}/Y_{138}	0,97806	5.0	0,92957	14.1	0,79844	16.1	0,66998
Y_{87}/Y_{138}	0,71654	37.9	0,44515	36.0	0,28503	17.2	0,23589
Y_{88}/Y_{138}	0,85724	29.5	0,60445	33.9	0,39964	20.3	0,31862
Y_{89}/Y_{138}	0,94446	26.8	0,69173	28.3	0,49569	25.6	0,369
Y_{87}/Y_{142}	0,89638	38.5	0,5129	39.3	0,33437	14.1	0,28735
Y_{88}/Y_{142}	1,0724	30.2	0,74857	37.4	0,46882	17.2	0,38813
Y_{89}/Y_{142}	1,18151	27.5	0,85666	32.1	0,5815	22.7	0,4495

Conclusions

As a result of the calculations, optimal pairs of light and heavy products (with close half-lives) of photofission of actinide nuclei ^{232}Th, ^{235}U, ^{238}U, ^{239}Pu were identified as potential sources of delayed gamma radiation and suitable for analysis of their isotopic composition. It has been demonstrated that combinations of numerical values of the ratio of the fields of light and heavy products (Y_{88}/Y_{135}, Y_{92}/Y_{135}, Y_{92}/Y_{138}, Y_{87}/Y_{138}, Y_{88}/Y_{138}, Y_{89}/Y_{138}, Y_{87}/Y_{142}, Y_{88}/Y_{142}, Y_{89}/Y_{142}) are substantially dependent on the mass of the fissile nuclei.

The calculations made make it possible to determine the ratio of the yields of light and heavy photofission products of actinide kernels for which no experimental data are available, and allow optimization of the procedure of non-destructive analysis of the isotope composition of unshielded and shielded fissile nuclear materials on electronic accelerators – microtron.

Acknowledgments

The authors express their gratitude to Full Doctor of Physical and Mathematical Sciences, Professor L.M. Suslikov for fruitful discussions and advice.

References

[1] Gozani T. Active non destructive assay of nuclear materials: Principles and applications. United States: National Technical Information Service; 1981. 403 p.
[2] Agarwal C, Chaudhury S, Nathaniel TN, Goswami A. Nondestructive assay of plutonium in empty stainless steel boxes by apparent mass method. *Radioanal Nucl Chem*. 2012;(294);77-80.
[3] De Stefano R, Carasco C, Pérot B, Simon E, Nicol T, Mauerhofer E. Feasibility study of fissile mass detection in 870 L radioactive waste drums using delayed gamma rays from neutron-induced fission. *J. Radioanal. Nucl. Chem.* 2019;(322):1185-94.
[4] Beddingfield DH, Cecil EE. Dentification of fissile materials from fission product gamma-ray spectra. *Nucl. Instr. Meth. A*. 1998;(417):405-12.
[5] Marrs RE, Norman EB, Burkeetal JT. Fission-product gamma-ray line pairs sensitive to fissile material and neutron energy. *Nucl. Instr. Meth. A*. 2008;(592):463-71.
[6] Iyengar A, Norman EB, Howard C, Angell C, Kaplan A, Ressler JJ, et al. Distinguishing fissions of ^{232}Th, ^{237}Np and ^{238}U with beta-delayed gamma rays. *Nucl. Instr. Meth. B*. 2013;(304):11-15.
[7] Hollas CL, Close DA, Moss CE. Analysis of fissionable material using delayed gamma rays from photofission. *Nucl. Instrum. Methods Phys.* 1987;24–25(1):503-505.
[8] Carrel F, Gmar M, Laine F, Loridon J, Ma J-L, Passard C. Identification of actinides inside nuclear waste packages by measurement of fission delayed gammas. *IEEE Nucl Sci Symp Conf Rec.* 2006;28(1):909-913.
[9] Carrel F, Agelou M, Gmar M, Lainé F, Loridon J, Ma J-L. Identification and differentiation of actinides inside nuclear waste packages by measurement of delayed gammas. *IEEE Trans. Nucl. Sci*. 2010;57(5):2862-71.
[10] Decay radiation search. Decay radiation database version of 12/2/2019.
[11] Schmidt K-H, Jurado B, Amouroux C, Schmitt C. General description of fission observables: GEF model code. *Nucl. Data Sheets.* 2016;(131):107-221.
[12] Pylypchynets IV, Parlag OO, Oleynikov EV. Simulation the yields of actinide nuclei photofission products induced by bremsstrahlung of electron accelerators. *Scientific Herald of Uzhhorod University. Series "Physics"*. 2017;(42):169-77.

[13] Bernard D, Serot O, Simon E, Boucher L, Plumeri S. Photofission delayed γ-ray spectra calculation tool for the conception of a nuclear material characterization facility. *EPJ Web of Conferences*. 2018:(170):06001.
[14] GEANT4 10.7 [Internet]. 2020. Available from: https://geant4.web.cern.ch/node/1899.
[15] Introduction to GEANT4 [Internet]. 2000. Available from: https://geant4.web.cern.ch/sites/geant4.web.cern.ch/files/geant4/support/training/CSC2000/CSCG4.pdf.
[16] Parlag OO, Maslyuk VT, Dovbnya AM, Pylypchynets IV, Golovey VM, Lendel OI, inventor; Institute of Electron Physics, National Academy of Sciences of Ukraine, patent owner. Method of stimulating delayed gamma radiation from fission products of actinide nuclei in sealed stainless steel containers for identification of their isotopic composition. Ukrainian patent for utility model No. 133090. 2019 Mar. 03.
[17] Evaluated Nuclear Data File (ENDF). Database Version of 2017-10-27.
[18] GEF 2020/1.1 [Internet]. 2020. Available from: http://www.khschmidts-nuclear-web.eu/GEF-2020-1-1.html.
[19] Piessens H, Jacobs E, De Frenne D, De Clercq A, Verboven M, De Smeet G. Photon induced fission of ^{232}Th with 12 and 20 MeV bremsstrahlung. In: Seeliger D, Seidel K, Marten H, editors. Proceeding of the XVth International Symposium on Nuclear Physics – Nuclear Fission; 1985 Nov. 11-15; Gaussig. Dresden: Technical University of Dresden; 1985. 92-95.
[20] Naik H, Kim GN, Schwengner R, Kim K, John R, Massarczyk R, et al. Fission product yield distribution in the 12, 14, and 16 MeV bremsstrahlung-induced fission of ^{232}Th. *Eur. Phys. J. A.* 2015;(51):150.
[21] Jacobs E, Thierens H, De Frenne D, De Clercq A, D'hondt P, De Gelder P, et al. Product yields for the photofission of ^{235}U with 12-,15-, 20-, 30-, and 70-MeV bremsstrahlung. *Phys. Rev. C.* 1980;21(1):237-45.
[22] Jacobs E, Thierens H, De Frenne D, De Clercq A, D'hondt P, De Gelder P, et al. Product yields for the photofission of ^{238}U with 12-, 15-, 20-, 30-, and 70-Mev bremsstrahlung. *Phys. Rev. C.* 1980;(19):422-32.
[23] Naik H, Carrel F, Kim GN, Laine F, Sari A, Normand S, et al. Mass yield distributions of fission products from photo-fission of ^{238}U induced by 11.5-17.3 MeV bremsstrahlung. *Eur. Phys. J. A* 2013;(49):94.
[24] England TR, Rider BF. Endf-349 evaluation and compilation of fission product yields 1993. Los Alamos: Los Alamos Nationatial Laboratory; 1994. 174 p.
[25] Nuclear Wallet Card Search. Nuclear Wallet Cards database version of 7/10/2019.

Список використаної літератури

[1] Gozani T. Active non destructive assay of nuclear materials: Principles and applications. United States: National Technical Information Service; 1981. 403 p.
[2] Agarwal C, Chaudhury S, Nathaniel TN, Goswami A. Nondestructive assay of plutonium in empty stainless steel boxes by apparent mass method. *Radioanal Nucl Chem*. 2012;(294);77–80.
[3] De Stefano R, Carasco C, Pérot B, Simon E, Nicol T, Mauerhofer E. Feasibility study of fissile mass detection in 870 L radioactive waste drums using delayed gamma rays from neutron-induced fission. *J. Radioanal. Nucl. Chem.* 2019;(322):1185–94.
[4] Beddingfield DH, Cecil EE. Dentification of fissile materials from fission product gamma-ray spectra. *Nucl. Instr. Meth. A*. 1998;(417):405–12.
[5] Marrs RE, Norman EB, Burkeetal JT. Fission-product gamma-ray line pairs sensitive to fissile material and neutron energy. *Nucl. Instr. Meth. A*. 2008;(592):463–71.
[6] Iyengar A, Norman EB, Howard C, Angell C, Kaplan A, Ressler JJ, et al. Distinguishing fissions of ^{232}Th, ^{237}Np and ^{238}U with beta-delayed gamma rays. *Nucl. Instr. Meth. B*. 2013;(304):11–15.
[7] Hollas CL, Close DA, Moss CE. Analysis of fissionable material using delayed gamma rays from photofission. *Nucl. Instrum. Methods Phys*. 1987;24–25(1):503–505.
[8] Carrel F, Gmar M, Laine F, Loridon J, Ma J-L, Passard C. Identification of actinides inside nuclear waste packages by measurement of fission delayed gammas. *IEEE Nucl Sci Symp Conf Rec*. 2006;28(1):909–913.
[9] Carrel F, Agelou M, Gmar M, Lainé F, Loridon J, Ma J-L. Identification and differentiation of actinides inside nuclear waste packages by measurement of delayed gammas. *IEEE Trans. Nucl. Sci*. 2010;57(5):2862–71.
[10] Decay radiation search. Decay radiation database version of 12/2/2019.
[11] Schmidt K-H, Jurado B, Amouroux C, Schmitt C. General description of fission observables: GEF model code. *Nucl. Data Sheets*. 2016;(131):107–221.
[12] Pylypchynets IV, Parlag OO, Oleynikov EV. Simulation the yields of actinide nuclei photofission products induced by bremsstrahlung of electron accelerators. *Scientific Herald of Uzhhorod University. Series "Physics"*. 2017;(42):169–77.
[13] Bernard D, Serot O, Simon E, Boucher L, Plumeri S. Photofission delayed γ-ray spectra calculation tool for the conception of a nuclear material characterization facility. *EPJ Web of Conferences*. 2018:(170):06001.
[14] GEANT4 10.7 [Internet]. 2020. Available from: https://geant4.web.cern.ch/node/1899.
[15] Introduction to GEANT4 [Internet]. 2000. Available from: https://geant4.web.cern.ch/sites/geant4.web.cern.ch/files/geant4/support/training/CSC2000/CSCG4.pdf.

[16] Парлаг ОО, Маслюк ВТ, Довбня АМ, Пилипчинець ІВ, Головей ВМ, Лендел ОІ, винахідник; Інститут електронної фізики НАН України, патентовласник. Спосіб стимуляції запізнілого гамма-випромінювання від продуктів поділу ядер актинідів в герметичних контейнерах із неіржавіючої сталі для ідентифікації їх ізотопного складу. Патент України на корисну модель № 133090. 2019 берез. 03.
[17] Evaluated Nuclear Data File (ENDF). Database Version of 2017-10-27.
[18] GEF 2020/1.1 [Internet]. 2020. Available from: http://www.khschmidts-nuclear-web.eu/GEF-2020-1-1.html.
[19] Piessens H, Jacobs E, De Frenne D, De Clercq A, Verboven M, De Smeet G. Photon induced fission of ^{232}Th with 12 and 20 MeV bremsstrahlung. In: Seeliger D, Seidel K, Marten H, editors. Proceeding of the XVth International Symposium on Nuclear Physics – Nuclear Fission; 1985 Nov. 11–15; Gaussig. Dresden: Technical University of Dresden; 1985. 92–95.
[20] Naik H, Kim GN, Schwengner R, Kim K, John R, Massarczyk R, et al. Fission product yield distribution in the 12, 14, and 16 MeV bremsstrahlung-induced fission of ^{232}Th. *Eur. Phys. J. A.* 2015;(51):150.
[21] Jacobs E, Thierens H, De Frenne D, De Clercq A, D'hondt P, De Gelder P, et al. Product yields for the photofission of ^{235}U with 12-,15-, 20-, 30-, and 70-MeV bremsstrahlung. *Phys. Rev. C.* 1980;21(1):237–45.
[22] Jacobs E, Thierens H, De Frenne D, De Clercq A, D'hondt P, De Gelder P, et al. Product yields for the photofission of ^{238}U with 12-, 15-, 20-, 30-, and 70-Mev bremsstrahlung. *Phys. Rev. C.* 1980;(19):422–32.
[23] Naik H, Carrel F, Kim GN, Laine F, Sari A, Normand S, et al. Mass yield distributions of fission products from photo-fission of ^{238}U induced by 11.5–17.3 MeV bremsstrahlung. *Eur. Phys. J. A* 2013;(49):94.
[24] England TR, Rider BF. Endf-349 evaluation and compilation of fission product yields 1993. Los Alamos: Los Alamos Nationatial Laboratory; 1994. 174 p.
[25] Nuclear Wallet Card Search. Nuclear Wallet Cards database version of 7/10/2019.

Розрахунок виходів продуктів фотоподілу ядер актинідів – джерел запізнілого гамма-випромінювання для потреб аналізу їх ізотопного складу

І.В. Пилипчинець, Є.В. Олейников, О.О. Парлаг

Інститут електронної фізики НАН України
88017, вул. Університетська, 21, м. Ужгород, Україна

Анотація

Мета. Одним з найважливіших завдань атомної промисловості є контроль за нерозповсюдженням ядерних матеріалів, що розщеплюються (наприклад, ^{232}Th, ^{235}U, ^{238}U, ^{239}Pu) на всіх етапах їх використання (переміщення, зберігання тощо). Для успішного вирішення цієї проблеми потрібна достовірна інформація про їх ізотопний склад. Метою дослідження є моделювання масових розподілів продуктів фотоподілу ядер ^{232}Th, ^{235}U, ^{238}U, ^{239}Pu, затримка гамма-випромінювання яких може бути використано для неруйнівного ізотопного аналізу ядерних матеріалів на прискорювачах електронів.

Методи. Розрахунки масових розподілів продуктів фоторозщеплення ядер ^{232}Th, ^{235}U, ^{238}U, ^{239}Pu було проведено із застосуванням GEF-коду. Спектр гальмівного випромінювання було змодельовано під час взаємодії електронів (E=12,5 МеВ) із танталовим перетворювачем (1 мм) за допомогою GEANT4 10.7.

Результати. Проведено моделювання масових розподілів продуктів фотоподілу ядер ^{232}Th, ^{235}U, ^{238}U, ^{239}Pu. Коефіцієнт виходів продуктів для ядерних пар (Y_{88}/Y_{135}, Y_{92}/Y_{135}, Y_{92}/Y_{138}, Y_{87}/Y_{138}, Y_{88}/Y_{138}, Y_{89}/Y_{138}, Y_{87}/Y_{142}, Y_{88}/Y_{142}, Y_{89}/Y_{142}) розраховуються для зазначених ядер. Оцінка різниці між числовими значеннями коефіцієнта виходу фрагментів пар для ядерних пар $_{232}$Th та $_{235}$U, $_{235}$U та $_{238}$U, $_{238}$U та $_{239}$Pu зроблено у відсотках. Значення різниці у співвідношеннях виходу цих пар продуктів становлять -5,0÷43,2 %, 14,1÷39,3 % та 14,1÷39,3 % для ядерних пар ^{232}Th та ^{235}U, ^{235}U та ^{238}U, ^{238}U і ^{239}Pu відповідно.

Висновки. Результати моделювання вказують на можливість використання зазначених вище пар продуктів поділу як джерел затримки гамма-випромінювання при проведенні неруйнівного ізотопного аналізу ядерних матеріалів. Отримані результати можуть бути використані для оптимізації експериментів на прискорювачах електронів, що підвищить точність та надійність результатів

Ключові слова: ядерні матеріали, ізотопний аналіз, фотоподіл, виходи продуктів, запізніле гамма-випромінювання

Расчет выходов продуктов фотоделения ядер актинидов – источников запаздывающего гамма-излучения для нужд анализа их изотопного состава

И.В. Пилипчинец, Е.В. Олейников, О.А. Парлаг

Институт электронной физики НАН Украины
88017, ул. Университетская, 21, г. Ужгород, Украина

Аннотация

Цель. Одной из важнейших задач атомной промышленности является контроль за нераспространением ядерных расщепляющихся материалов (например, ^{232}Th, ^{235}U, ^{238}U, ^{239}Pu) на всех этапах их использования (перемещение, хранение и т.д.). Для успешного решения этой проблемы нужна достоверная информация об их изотопном составе. Целью исследования является моделирование массовых распределений продуктов фотоделения ядер ^{232}Th, ^{235}U, ^{238}U, ^{239}Pu, задержка гамма-излучения, которое может быть использовано для неразрушающего изотопного анализа ядерных материалов на ускорителях электронов.

Методы. Расчеты массовых распределений продуктов фоторасщепления ядер ^{232}Th, ^{235}U, ^{238}U, ^{239}Pu было проведено с применением GEF-кода. Спектр тормозного излучения было смоделировано при взаимодействии электронов (E=12,5 МэВ) с танталовым преобразователем (1 мм) с помощью GEANT4 10.7.

Результаты. Проведено моделирование массовых распределений продуктов фотоделения ядер ^{232}Th, ^{235}U, ^{238}U, ^{239}Pu. Коэффициент выходов продуктов для ядерных пар (Y_{88}/Y_{135}, Y_{92}/Y_{135}, Y_{92}/Y_{138}, Y_{87}/Y_{138}, Y_{88}/Y_{138}, Y_{89}/Y_{138}, Y_{87}/Y_{142}, Y_{88}/Y_{142}, Y_{89}/Y_{142}) рассчитываются для указанных ядер. Оценка разницы между числовыми значениями коэффициента выхода фрагментов пар для ядерных пар ^{232}Th и ^{235}U, ^{235}U и ^{238}U, ^{238}U и ^{239}Pu сделано в процентах. Значение разницы в соотношениях выхода этих пар продуктов составляют 5,0÷43,2 %, 14,1÷39,3 % и 14,1÷39,3 % для ядерных пар ^{232}Th и ^{235}U, ^{235}U и ^{238}U, ^{238}U и ^{239}Pu соответственно.

Выводы. Результаты моделирования указывают на возможность использования указанных выше пар продуктов деления как источников задержки гамма-излучения при проведении неразрушающего изотопного анализа ядерных материалов. Полученные результаты могут быть использованы для оптимизации экспериментов на ускорителях электронов, что повысит точность и надежность результатов

Ключевые слова: ядерные материалы, изотопный анализ, фотоделение, выходы продуктов, запаздывающее гамма-излучение

Scientific Herald of Uzhhorod University
Series "Physics"

Journal homepage: https://physics.uz.ua/en
Issue 48, 50-57
Received: 16.08.2020. Revised: 10.11.2020. Accepted: 15.12.2020

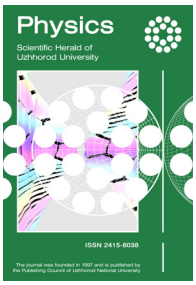

УДК 539.172.4
PACS 25.40.Fq, 06.20.Dk, 29.30.−h
DOI: 10.24144/2415-8038.2020.48.50-57

Enhancement of Gamma-Ray Yield from Fast Neutrons Interaction with Cadmium Isotopes

B.M. Bondar[1,2*], B.Yu. Leshchenko[2], I.M. Kadenko[1]

[1]Taras Shevchenko National University
01601, 64/13 Volodymyrska Str., Kyiv, Ukraine

[2]National Technical University of Ukraine "Igor Sikorsky Kyiv Polytechnic Institute"
03056, 37 Peremohy Ave., Kyiv, Ukraine

Abstract

Purpose. This paper presents the results of investigation of γ-ray yield enhancement from ^{nat}Cd(n, $x\gamma$) reactions obtained in experiments with 14-MeV neutrons in comparison with theoretical spectrum calculated in Empire code.

Methods. The experiment was carried out applying TOF-technique for n-γ discrimination. The MCNP simulation of the experiment was performed and the influence of scattered neutrons background at gamma-ray spectrum shape was estimated.

Results. It was shown that despite TOF-technique thermal neutrons capture by ^{113}Cd isotope gives considerable contribution to gamma-spectrum induced in ^{nat}Cd sample by primary DT-neutrons. The thermal neutron flux was determined to be nearly constant at different locations of experimental hall.

Conclusions. For the correct measurements of the γ-production cross sections for cadmium samples the sufficient separation between primary neutrons and scattered ones must be provided

Keywords: thermal neutrons, DT-neutrons, cadmium, gamma-spectrum, gamma-ray yield

Introduction

The cross sections of gamma-rays production induced by neutron interactions are required for radiation damage and shielding calculations of the fission and fusion reactors. The 14-MeV neutrons are of utmost importance for these tasks because of the big number of open reaction channels at this incident neutrons energy. Almost all of interactions between neutrons and nuclei of interest are accompanied by the prompt gammas emission, and the (n, $x\gamma$) reactions cross sections must be precisely known for the modern and future reactor construction elements undergoing neutron exposure. Despite large number of experiments performed with DT-neutrons they

Suggested Citation:
Bondar BM, Leshchenko BYu, Kadenko IM. Enhancement of gamma-ray yield from fast neutrons interaction with Cadmium isotopes. *Scientific Herald of Uzhhorod University. Series "Physics"*. 2020;(48):50-57.

*Corresponding author

are still relevant for fusion reactors design. It is caused by disagreements between nuclear data from different authors [1] or between experimental results and theoretical calculations. In particular, the last ones were obtained in our experiments for Cd element [2], which is commonly used in the reactors industry. The measured gamma-ray spectrum appeared to be enhanced in comparison with theoretical calculations. In this work we present the investigation of this phenomenon.

Data Analysis

Our experiments in gamma-ray spectroscopy were performed with 14-MeV neutrons for different samples, such as ^{nat}Fe, ^{nat}Bi, ^{nat}Cd, ^{nat}Ni, ^{nat}Sn and ^{nat}C [2-5]. All the measurements were carried out using the pulse neutron generator facility PNG-200 under the same geometry (samples had the torus shapes with outer and inner radii of 10÷16.5 cm and 1.5 cm, respectively) and with the same settings: for n-γ discrimination the time-of-flight (TOF) technique was applied with pulse repetition period (PRP) of 140 ns and with γ-detection time window of 20 ns (the detailed description of experiments and DAQ can be found in [4]). A good agreement between experimental results and theoretical calculations performed in Empire code [6] was obtained for all elements except natCd sample, where notable discrepancy in the 5÷10 MeV energy range is observed (Fig. 1). Such enhancement of measured gamma-spectrum from ^{nat}Cd was also observed in works of other authors [7; 8].

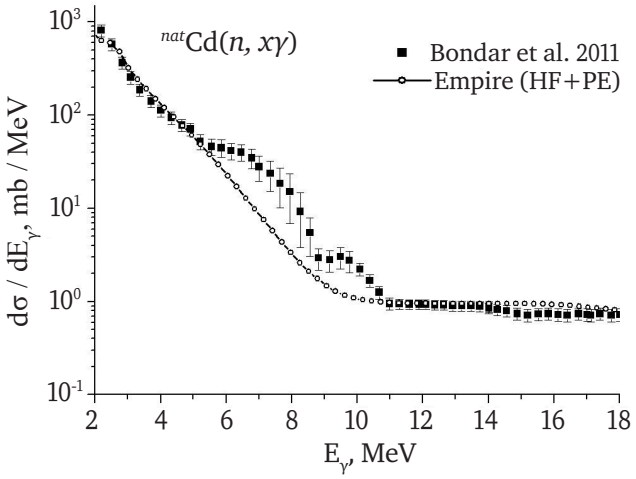

Figure 1. The experimental data and theoretical calculations of gamma-ray spectrum from ^{nat}Cd(n, $x\gamma$) reactions induced by 14-MeV neutrons

The origin of this discrepancy can be caused by the experimental conditions such as presence of thermal neutrons background. The neutron scattering on construction elements and walls of the experimental hall leads to continuous neutron spectrum formation in the experimental hall, as well as the sample itself, and takes much longer than PRP time. Hence, despite TOF technique, the background gammas induced by low-energy neutrons interaction can also be detected in the time window. It is well-known that for ^{nat}Fe, ^{nat}Bi, ^{nat}Ni, ^{nat}Sn and ^{nat}C elements capture cross section even for thermal neutrons does not exceed several barns. But for ^{nat}Cd this value is about 2500 b, and (n, γ) reactions can cause an essential impact on gamma-ray spectrum.

An additional contribution to γ-spectrum is mainly expected to be from the ^{113}Cd(n, γ) ^{114}Cd nuclear reaction. The ^{113}Cd isotope has 12.23% in natural abundance and average cross section of 20 000 b for thermal neutrons capture resulting in formation of compound nucleus ^{114}Cd with excitation energy 9.04 MeV. The de-excitation of this state occurs with high probability by the

cascade E2 transitions through the discrete levels 0-558.45 keV-1283.7 keV-1991 keV-2670 keV, accompanied by gamma-rays with the energies 9.04 MeV, 8.48 MeV, 7.76 MeV, 7.05 MeV, and 6.37 MeV (Fig.2).

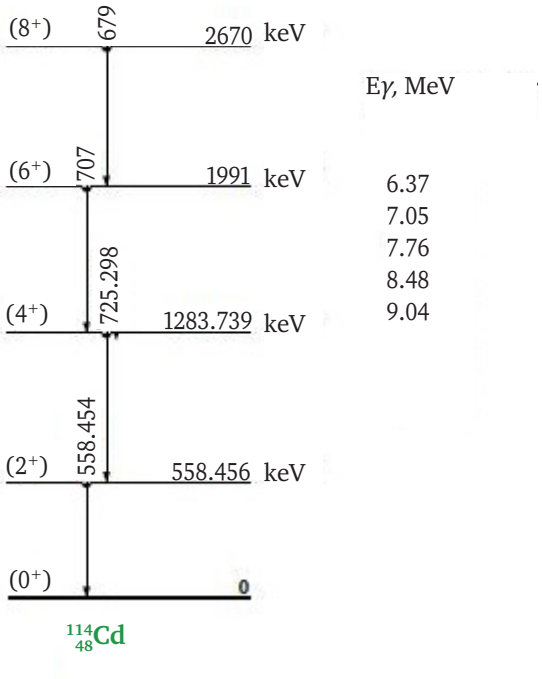

Figure 2. Possible γ-transitions from the $^{113}Cd(n, \gamma)\ ^{114}Cd$ reactions at excitation energy of 9.04 MeV

The energy resolution for these energies in experiment was near 1 MeV, so along with continuum transitions these gamma-rays due to neutron capture could provide smooth enhancement of gamma-spectrum within the energy interval 5÷10 MeV. The continuum transitions from $^{113}Cd(n, \gamma)^{114}Cd$ reactions give notable contribution below 7 MeV [9], therefore the observed double-humped spectrum can be formed by the sum of a group of peaks around 7 MeV and the continuous spectrum increasing at lower energies (left part), and discrete gamma-rays with energies from 7.05 to the 9.04 MeV in the right part of the spectrum. All these considerations indicate possible influence of low-energy neutrons. To figure this out, the scattered neutrons fluxes must be determined.

MCNP Simulations

The 14-MeV and thermal neutrons fluxes were estimated by MCNP [10] simulations. The geometry of the experiment is presented in Figure 3. The main components that can effectively moderate neutrons, such as concrete walls, floor, roof and oil filled bucket for high voltage supply were also built for simulations.

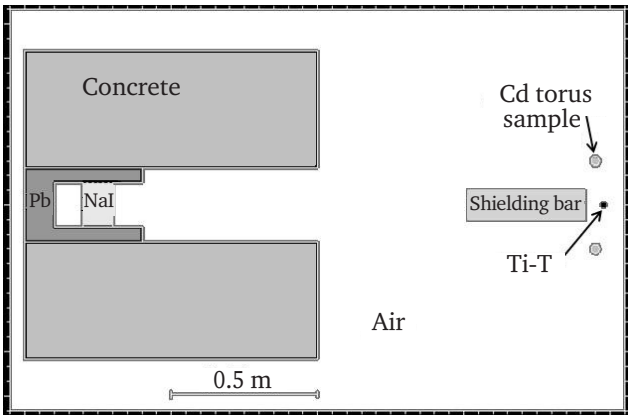

Figure 3. The MCNP geometry of the experiment

The overall time of neutrons moderation to the thermal energies and subsequent diffusion before absorption is several hundreds of

microseconds. The PNG-200 generates pulses of DT-neutrons with period of 0.14 μs, so it can be considered as constant neutrons source relative to the scattered neutrons lifetime in experimental hall. In such conditions the flux of thermal neutrons is statistically averaged and nearly constant during the measurements with strong dependence on intensity of DT-neutrons from the Ti-T target. Therefore the continuous and isotropic point-source of 14-MeV neutrons was specified in simulations.

The neutrons fluxes per one DT-neutron from the source were determined at different locations in the experimental hall: near the sample, behind the shielding bar and near the wall, which is at 3.5 m distance from Ti-T target. The results of simulated fluxes are shown in Table 1.

Table 1. Primary 14-MeV and scattered low-energy (0÷0.5 eV) neutron fluxes at different locations

Location	F_{14}, 1/cm²/DT – neutron (14 MeV)	F_{th}, 1/cm²/DT – neutron (0÷0.5 eV)
Near the sample	$2.92 \cdot 10^{-4}$	$9.66 \cdot 10^{-7}$
Behind shielding bar	$9.57 \cdot 10^{-6}$	$9.48 \cdot 10^{-7}$
Near the wall	$7.59 \cdot 10^{-7}$	$9.65 \cdot 10^{-7}$

The simulated neutron spectra near the sample within the 0.1÷15 MeV and 0÷0.5 eV energy ranges are shown in Figure 4 The ratio between 14-MeV (F_{14}) and thermal (from 0 and up to 0.5 eV, F_{th}) neutron fluxes near the sample appeared to be F_{14}/F_{th}=302.3.

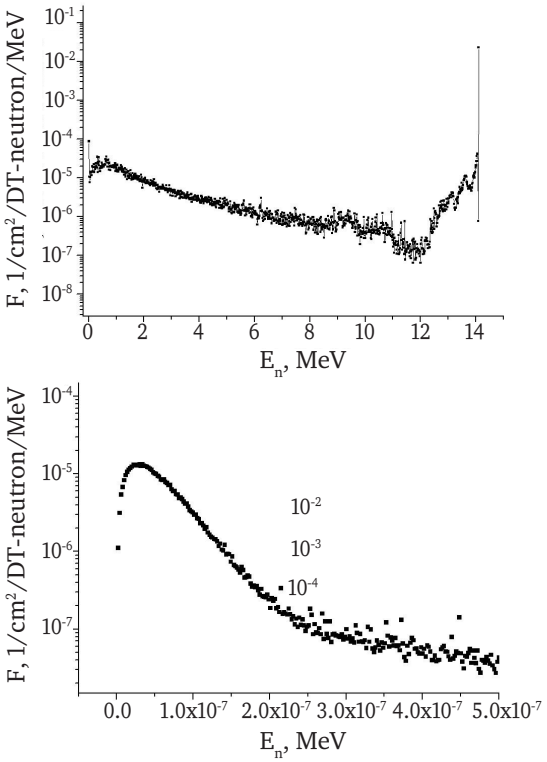

Figure 3. Simulated neutron spectra near the ^{nat}Cd sample

The yield of gamma-rays from (n, xγ) reactions induced by 14-MeV neutrons in the ^{nat}Cd sample equals (1):

$$Y_{14} = N_{14} F_{14} \alpha_n \sigma_{14} \quad (1)$$

where N_{14} is the number of nuclei undergoing irradiation by 14 MeV neutrons; F_{14} is the 14-MeV neutron fluence; αn – coefficient for 14-MeV neutrons beam attenuation in the sample; σ_{14} – cross section of gamma-production from (n, $x\gamma$) reactions induced by 14-MeV neutrons. In case of thermal neutrons, the high cross section of radiative capture by ^{113}Cd isotope limits the free path of thermal neutron in cadmium by the value of $\lambda_{th}=1/\Sigma_{th}=8.6*10^{-3}$ cm. As a result, all the thermal neutrons are absorbed within a thin ($x<$ 0.1cm) layer of cadmium, and (n, γ) reactions rate equals to the total number of neutrons hitting the torus sample (2):

$$R_{14} = F_{th}(1 - exp\,(-x\,/\,\lambda_{th}))S = F_{th}S \quad (2)$$

Here S is the area of the sample surface, and $(1 - exp(-x/\lambda_{th})$ determines the neutrons attenuation at distance x inside the sample. The gamma-yield caused by thermal neutrons Y_{th} is the product of capture reactions rate R_{th} and multiplicity of capture γ-rays M_γ. During experiments the total yield $Y_{exp}=Y_{14}+Y_{th}$ is measured including both thermal and 14-MeV neutrons induced reactions, and the enhancement of gamma-yield caused by thermal neutrons contribution can be expressed as follows (3):

$$\frac{Y_{exp}}{Y_{14}} = 1 + \frac{Y_{th}}{Y_{14}} = 1 + \frac{F_{th} S M_\gamma}{N_{14} F_{14} \alpha_n \sigma_{14}} \quad (3)$$

While the measured cross section of gamma-ray production σ_{exp} is proportional to the yield Y_{exp} (because Y_{th} was normalized to $N_{14}F_{14}$), and the response function of the spectrometer is the same for gamma-rays of different origins, the relation between different gamma-production cross sections correlates with corresponding yields. The cross section discrepancy between measured experimental data and theoretical calculations in the 5÷10 MeV energy range is (4):

$$\frac{\int_5^{10} \frac{d\sigma_{exp}}{dE} dE}{\int_5^{10} \frac{d\sigma_{14}}{dE} dE} = 1.64 \pm 0.18 \quad (4)$$

while equation (3) gives close to this discrepancy value between experimental and theoretical yields (5):

$$1 + \frac{F_{th} S M_\gamma N_{\gamma th}}{N_{14} F_{14} \alpha_n \sigma_{14} N_{\gamma 14}} = 1.47 \quad (5)$$

Here M_γ=4.1 is average gamma-ray multiplicity of ^{113}Cd(n, γ)^{114}Cd reactions, $N_{\gamma th}$=10.2% is part of gamma-spectrum within considered energy range induced by thermal neutrons [11] and $N_{\gamma 14}$=2.2% is the same for 14-MeV neutrons obtained from Empire calculations.

The values in (4) and (5) confirm the idea of contribution from thermal neutrons to the measured spectrum. The excess of the measured gamma-production cross section within 5÷10 MeV is 60 mb, and one could assume that it is caused not by 14-MeV, but thermal neutrons interactions with ^{113}Cd nuclei. Then the cross section of gamma-ray production renormalized to the flux of thermal neutrons and number of ^{113}Cd nuclei equals 11 450 barn, which makes 12.7% of the total cross section of gamma-yield, namely 88 000 b [11].

The value obtained in (5) shows that the number of gamma-rays generated by thermal neutrons is about 47% of gamma-rays from 14-MeV neutrons and it is comparable with obtained discrepancy (4). Obviously, this contribution must be taken into account during gamma-spectra measurements from fast neutrons interactions. It can be seen from table 1 that the primary 14-MeV neutrons beam near the sample is bigger than at other locations by 30 (behind the shielding bar) and 385 (near the wall) times respectively, while the thermal neutrons flux is nearly constant regardless of the location of control volume in the experimental hall. It means that the changing of the sample position will not reduce the influence from scattered neutrons and the additional

shielding is required. In particular, it can be realized with the help of neutronstop covering on walls, ceiling and floor. According to MCNP simulations, such type of shielding (with bricks of 10 cm thickness and 5% of ^{10}B addition by mass) leads to the reduction of thermal neutrons flux up to 10^2 times. But the clear gamma-spectra from 14-MeV neutrons can be obtained only taking into account the scattered ones.

Despite values in (4) and (5) are close, the experimental enhancement is still higher than expected one from thermal neutrons. This bump was also observed in the experiments with high flux of thermal neutrons and enriched ^{113}Cd sample in [11], and it could not be reproduced by theoretical calculations. So this energy region is under the interest and requires additional investigations.

Conclusions

It was shown that the discrepancy in the gamma-spectrum from natCd sample is caused by the thermal neutrons interactions due to the big capture cross section with ^{113}Cd nuclei. The MCNP simulations confirmed this idea and helped to understand the irradiation conditions of the experiment. According to obtained results, about 30% of all gamma-rays from (n, $x\gamma$) reactions induced in the ^{nat}Cd sample caused by thermal neutrons, and the flux of them is nearly constant at different points in the experimental hall. Therefore, the measurements of fast neutrons interactions with cadmium samples must be conducted very carefully taking into account possible contributions from thermal neutrons. The best way is to ensure the irradiation conditions with minimum scattered and maximum of 14-MeV neutrons fluxes and to provide sufficient separation between them. Our further investigation includes reexamination of gamma-production cross sections of ^{nat}Cd(n, $x\gamma$) reactions induced by 14-MeV neutrons.

References

[1] Simakov SP, Pavlik A, Vonach H, Hlavac S. Status of experimental and evaluated discrete γ-ray production at En=14.5 MeV. Vienna: International Atomic Energy Agency; 1998. 60 p.

[2] Bondar BM, Bondar VM, Gorbachenko OM, Kadenko IM, Leshchenko BYu, Onishchuk YuM, et al. Cross sections of prompt γ-ray production induced by interactions of fast neutrons with cadmium. *Nucl. Phys. At. Energy*. 2011;12(2):129-36.

[3] Bondar VM, Gorbachenko OM, Kadenko IM, Leshchenko BYu, Onishchuk YuM, Plujko VA. Spectra of gamma-rays in (n,xγ) reactions on ferrum and bismuth nuclei. *Nucl. Phys. At. Energy.* 2010;11(3):246-50.

[4] Kadenko IM, Plujko VA, Bondar BM, Gorbachenko OM, Leshchenko BYu, Solodovnyk KM. Prompt gamma-rays from fast neutron capture in ^{nat}Ni. *Nucl. Phys. At. Energy.* 2016;17(2):122-29.

[5] Kadenko IM, Plujko VA, Bondar BM, Gorbachenko OM, Leshchenko BYu, Solodovnyk KM. Gamma-rays from ^{nat}Sn and ^{nat}C induced by fast neutrons. *Nucl. Phys. At. Energy.* 2016;17(4):349-53.

[6] Herman M, Capote R, Carlson BV, Oblozinsky P, Sin M, Trkov A, et al. EMPIRE: Nuclear reaction model code system for data evaluation. *Nucl. Data Sheets.* 2007;108(12):2655-715.

[7] Bezotosnyy VM, Gorbachev VM, Surov LM, Shvetsov MS. Differential and total cross sections for gamma-production by inelastic interaction of 14 MeV neutrons with different nuclei. *PAST.* 1978;3(30):21-8.

[8] Nefedov YuYa, Nagornyj VI, Semenov VI. The experimental results of the gamma-ray production cross-section and spectra at the nonelastic interaction 14 MeV neutrons with nuclei of Na, S, Cl, Ti, V, Cr, Ni, Zn, Ge, Nb, Cd, In, Sn, Bi, ^{235}U and ^{238}U. *PAST*. 2000;(1):7-10.

[9] Rusev G, Jandel M, Krtiˇcka M, Arnold CW, Bredeweg TA, Couture A, et al. Cascade γ-rays following capture of thermal neutrons on ^{113}Cd. *Phys. Rev. C.* 2013;88(5):057602.
[10] RSICC Computer code collection. MCNP4C. Monte Carlo N particle transport code system. United States: Oak Ridge National Laboratory; 2000. 898 p.
[11] Belgya T, Szentmiklósi L, Massarczyk R, Schwengner R, Junghans AR, Grosse E. High-resolution study of the ^{113}Cd(n, γ) spectrum by statistical decay model with discrete levels and transitions. *EPJ Web Conf.* 2017;(146):05009.

Список використаної літератури

[1] Simakov SP, Pavlik A, Vonach H, Hlavac S. Status of experimental and evaluated discrete γ-ray production at En=14.5 MeV. Vienna: International Atomic Energy Agency; 1998. 60 p.
[2] Бондар БМ, Бондар ВМ, Горбаченко ОМ, Каденко ІМ, Лещенко БЮ, Оніщук ЮМ, та ін. Диференціальні перерізи вильоту гамма-квантів при взаємодії нейтронів з ядрами кадмію. *Ядерна фізика та енергетика*. 2011;12(2):129–36.
[3] Бондар ВМ, Горбаченко ОМ, Каденко ІМ, Лещенко БЮ, Оніщук ЮМ, Плюйко ВА. Спектри гамма-квантів у (*n,xγ*) реакціях на ядрах заліза та вісмуту. *Ядерна фізика та енергетика.* 2010;11(3):246–50.
[4] Каденко ІМ, Плюйко ВА, Бондар БМ, Горбаченко ОМ, Лещенко БЮ, Солодовник КМ. Миттєві гамма-кванти при поглинанні швидких нейтронів ядрами ^{nat}Ni. *Ядерна фізика та енергетика*. 2016;17(2):122–29.
[5] Каденко ІМ, Плюйко ВА, Бондар БМ, Горбаченко ОМ, Лещенко БЮ, Солодовник КМ. Гамма-випромінювання з ^{nat}Sn та ^{nat}C під дією нейтронів. Ядерна фізика та енергетика. 2016;17(4):349–53.
[6] Herman M, Capote R, Carlson BV, Oblozinsky P, Sin M, Trkov A, et al. EMPIRE: Nuclear reaction model code system for data evaluation. *Nucl. Data Sheets.* 2007;108(12):2655–715.
[7] Безотосный ВМ, Горбачев ВМ, Суров ЛМ, Швецов МС. Полные сечения образования γ-квантов при неупругом взаимодействии 14-МеВ нейтронов с различными ядрами. *Вопросы атомной науки и техники, серия ядерные константы*. 1978;3(30):21–8.
[8] Нефедов ЮЯ, Нагорный ВИ, Семенов ВИ, Житник АК, Орлов РА, Шмаров АЕ. Результаты измерений сечений и спектров образования гамма-квантов при неупругом взаимодействии 14 МэВ нейтронов с ядрами Na, S, Cl, Ti, V, Cr, Ni, Zn, Ge, Nb, Cd, In, Sn, Bi, ^{235}U and ^{238}U. *Вопросы атомной науки и техники, серия ядерные константы*. 2000;(1):7–10.
[9] Rusev G, Jandel M, Krtiˇcka M, Arnold CW, Bredeweg TA, Couture A, et al. Cascade γ rays following capture of thermal neutrons on ^{113}Cd. *Phys. Rev. C.* 2013;88(5):057602.
[10] RSICC Computer code collection. MCNP4C. Monte Carlo N particle transport code system. United States: Oak Ridge National Laboratory; 2000. 898 p.
[11] Belgya T, Szentmiklósi L, Massarczyk R, Schwengner R, Junghans AR, Grosse E. High-resolution study of the ^{113}Cd(n, γ) spectrum by statistical decay model with discrete levels and transitions. *EPJ Web Conf.* 2017;(146):05009.

Підсилення виходу гамма-квантів при взаємодії швидких нейтронів з ізотопами кадмію

Б.М. Бондар[1,2], Б.Ю. Лещенко[2], І.М. Каденко[1]

[1]Київський національний університет імені Тараса Шевченка
01601, вул. Володимирська, 64/13, м. Київ, Україна

[2]Національний технічний університет України
«Київський політехнічний інститут імені Ігоря Сікорського»
03056, просп. Перемоги, 37, м. Київ, Україна

Анотація

Мета. У цій статті представлено результати дослідження збільшення виходу гамма-випромінювання від реакцій ^{nat}Cd($n,x\gamma$), що було отримано під час експерименту з нейтронами з енергією 14-МеВ, порівняно з теоретичним спектром, розрахованим у коді Empire.

Методи. Експеримент проведено з застосуванням часопрольотної методики вимірювань для n-γ дискримінації. За допомогою MCNP симуляції було виконано експеримент й оцінено вплив фону від розсіяних нейтронів на форму гамма-спектру.

Результати. Було показано, що незважаючи на часову сепарацію подій, захват теплових нейтронів ізотопом ^{113}Cd дає суттєвий внесок у гамма-спектр із реакцій ^{nat}Cd($n, x\gamma$), зумовлених прямими DT-нейтронами. Було визначено флюенс теплових нейтронів, який виявився сталим у різних точках експериментальної зали.

Висновки. Для коректного вимірювання перерізів виходу гамма-квантів для зразків кадмію необхідно забезпечувати додаткову сепарацію між прямими та розсіяними нейтронами

Ключові слова: теплові нейтрони, DT-нейтрони, кадмій, гамма-спектр, гамма-вихід

Усиление выхода гамма-квантов при взаимодействии быстрых нейтронов с изотопами кадмия

Б.М.Бондар[1,2], Б.Е. Лещенко[2], И.Н. Каденко[1]

[1]Киевский национальный университет имени Тараса Шевченко
01601, ул. Владимирская, 64/13, г. Киев, Украина

[2]Национальный технический университет Украины
«Киевский политехнический институт имени Игоря Сикорского»
03056, просп. Победы, 37, г. Киев, Украина

Анотація

Цель. В этой статье представлены результаты исследования увеличения выхода гамма-излучения от реакций ^{nat}Cd ($n, x\gamma$), что были получены в ходе эксперимента с нейтронами с энергией 14-МэВ по сравнению с теоретическим спектром, рассчитанным в коде Empire.

Методы. Эксперимент проведен с применением часопролётной методики измерений для n-γ дискриминации. С помощью MCNP симуляции было выполнено эксперимент и оценено влияние фона от рассеянных нейтронов на форму гамма-спектра.

Результаты. Было показано, что несмотря на временную сепарацию событий, восторг тепловых нейтронов изотопом ^{113}Cd дает существенный вклад в гамма-спектр с реакций ^{nat}Cd ($n, x\gamma$), обусловленных прямыми DT-нейтронами. Было определено флюенс тепловых нейтронов, который оказался устойчивым в разных точках экспериментальной залы.

Выводы. Для корректного измерения сечений выхода гамма-квантов для образцов кадмия необходимо обеспечивать дополнительную сепарацию между прямыми и рассеянными нейтронами

Ключевые слова: тепловые нейтроны, DT-нейтроны, кадмий, гамма-спектр, гамма-выход

Scientific Herald of Uzhhorod University
Series "Physics"

Journal homepage: https://physics.uz.ua/en
Issue 48, 58-66
Received: 17.07.2020. Revised: 10.11.2020. Accepted: 15.12.2020

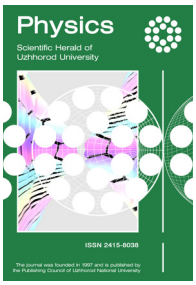

УДК 539.184.5
PACS 34.80.Dp, 34.80.Gs
DOI: 10.24144/2415-8038.2020.48.58-66

Theoretical Calculations of Electron Excitation of the Lowest Autoionization States of the Rb Atom

V.I. Roman, O.M. Pop, I.V. Pylypchynets*

Institute of Electron Physics, NAS of Ukraine
88017, 21 Universitetska Str., Uzhhorod, Ukraine

Abstract

Purpose. The value of the autoionization cross section and its energy dependence are determined to a great extent by excitation and subsequent electron decay of the lowest energy states. Recently, experimental data on the excitation cross sections of the rubidium atom lowest doublet $(4p^5 5s^2)^2P_{3/2,1/2}$ and quartet $(4p^5 4d5s)^4P_{1/2,3/2,5/2}$ autoionizing states were obtained which promoted their theoretical investigations.

Methods. Theoretical calculations were performed using the Flexible Atomic Code universal program package which takes account of the relativistic nature of the complex atoms excitation by the use of the Dirac-Coulomb Hamiltonian. The radial orbitals for basic relativistic wavefunctions were obtained by solving the Dirac-Fock-Slater equation.

Results. Comparison of the experimental excitation cross sections for the doublet $(4p^5 5s^2)^2P_{3/2,1/2}$ and quartet $(4p^5 4d5s)^4P_{1/2,3/2,5/2}$ autoionizing states with available theoretical data and our relativistic calculations is presented. The results of the study of the parameter R_0 for the intensity ratio for the $^2P_{3/2}$ and $^2P_{1/2}$ states of the $4p^5 5s^2$ configuration are presented. Our calculations in the distorted waves approximation is shown to well describe the experimental data in the energy region above 70 eV. At low collision energies our calculations qualitatively predict the presence of the threshold resonant excitation; however in the energy region 20-50 eV only the R-matrix method qualitatively describes the complex nature of excitation and decay of the lowest quartet autoionizing states of the rubidium atom.

Conclusions. Electron excitation of the doublet $(4p^5 5s^2)^2P_{3/2,1/2}$ and quartet $(4p^5 4d5s)^4P_{1/2,3/2,5/2}$ autoionizing states of the rubidium atom in the collision energy range from the excitation thresholds up to 700 eV was studied in the terms of the distorted waves relativistic approximation. A comprehensive analysis of the obtained results using the available experimental and theoretical data showed that the relativistic distorted waves approximation taking into account the configurational mixing is a suitable tool for describing the autoionizing states of the rubidium atom in a wide range of collision energies and allowed one to obtain the absolute values of the experimental excitation cross sections of the $(4p^5 5s^2)^2P_{3/2,1/2}$ and $(4p^5 4d5s)^4_{P1/2,3/2,5/2}$ states.

This work was supported by the grant program the project of young scientists of the National Academy of Sciences of Ukraine "Dynamics of formation of excited states of atoms and ions in plasma on a pair of metals: mechanisms of elementary processes"

Keywords: atom, electron impact excitation, autoionizing states, excitation cross section

Suggested Citation:
Roman VI, Pop OM, Pylypchynets IV. Theoretical calculations of electron excitation of the lowest autoionization states of the Rb atom. *Scientific Herald of Uzhhorod University. Series "Physics"*. 2020;(48):58-66.

*Corresponding author

Introduction

The charge composition and energy balance of various plasma media are mainly determined by two processes – direct ionization and autoionization. As has been shown in studies of these processes in heavy atoms of potassium, rubidium and caesium [1], the contribution of autoionization to the total electron shock ionization cross-section is more than 30%. Studies of these atoms have also shown that the size of the autoionization cross-section and the form of its energy dependence at low and high collision energy values are largely determined by the excitation and subsequent electronic decay of the lowest-energy states $np^5(n+1)s^2\ ^2P_{3/2,1/2}$ and $np^5nd(n+1)s\ ^4P_{1/2,3/2,5/2}$ (n=3, 4, 5 for K, Rb, Cs, respectively) [2-4].

It is known that the most complete information about the set of processes involved in the formation of a certain excited atomic state, namely the type of electron transition, cascade population, and the formation of negative ion resonances, is provided by the energy dependence of its excitation cross-section. Recently, by the method of electron spectroscopy using the technique of electron-atom beams, it was possible to experimentally obtain cross sections of the excitation of the lowest autoionization states (AIS) for the Rb atom [5-7]. Due to the significant spin-orbit splitting of levels in the Rb atom, apart from the doublet states $(4p^55s^2)^2P_{3/2,1/2}$ [5], in the study [6] the electronic excitation of each component with J=1/2, 3/2, 5/2 of quartet state $(4p^54d5s)^4$RJ was also studied. Detailed analysis of the near-threshold resonant structure of AIC data performed by the authors in the study [8]. In it, on the basis of theoretical calculations by the method of R-matrix with B-splines show that the resonant structure at the excitation cross-sections for $(4p^55s^2)^2P_{3/2,1/2}$ AIC is the result of a superposition of several states of the negative rubidium ion, and it is also established that almost all resonances are Feshbach-type resonances. As for the quartet AIC, the authors of the study [8] presented the excitation cross-sections of these AIC in the collision energy range up to 50 eV, but they were unable to identify the states of the negative rubidium ion due to the complexity of the excitation and decay mechanism of these AIC.

As for collision energies above 50 eV, only one theoretical work has been known so far [9], where the excitation cross-sections are presented and the role of $np^5(n+1)s^2\ ^2P_{3/2,1/2}$ AIC in the process of ionization of neutral alkaline atoms by electron shock. In this research, relativistic calculations of effective excitation cross-sections in the Born approximation and distorted waves (PCX) are performed, multiplet splitting analysis is performed, and the ratio of the cross-sections of the lowest doublet AIC of alkaline Na, K, Rb, and Cs atoms at different energies of the incident electron from the excitation thresholds to 1.5 keV is established, but without comparison with experimental data for Rb and Cs atoms. For quartets $(4p^54d5s)^4$RJ AIS theoretical data on excitation cross-sections for collision energies above 50 EV were not available.

In this study, we present the results of a theoretical study of the electron excitation of the lowest doublet and quartet autoionization states of a rubidium atom in a wide range of collision energies from excitation thresholds to 700 eV by the method of relativistic distorted waves, taking into account configuration mixing (the PCX-BK approximation) and without it (the PCX approximation) in comparison with the available theoretical and experimental data.

Research Methodology

Theoretical calculations were performed using the universal Flexible Atomic Code software package [10], which takes into account the relativistic nature of the excitation of complex atoms by using the Dirac-Coulomb Hamiltonian. This software package has proven itself well in the theoretical classification of AIC of the rubidium atom in the research [11], as well as in the study

of the excitation cross-section $4p^6$ shells of the Rb atom [12; 13].

It should be noted that the accuracy of the theoretical results obtained significantly depends on how the single-electron functions of the target are calculated and what configurations are mixed with each other. Clearly, there is no universal recipe for how to improve the results of calculations, it all depends on successful and complete consideration of configuration mixing. At the same time, the number of configurations cannot be excessively large, since it is impossible to take into account the interaction of an incoming electron with all possible configurations. Mixing of configurations is usually the largest when the energies of different configurations are close to each other, it can disrupt serial patterns and even change the nature of the multiplet separation of levels. Therefore, taking into account configuration mixing in such cases often leads to significant changes in the probability of decay of individual AIC, especially for weak transitions.

Radial orbitals for constructing basic relativistic wave functions were obtained by solving the Dirac-Fock-Slater equation. The set of configurations was somewhat reduced in comparison with [11], as our research showed that the best description of experimental excitation cross-sections is given by the inclusion of correlation corrections in the calculations of our selected configurations, although excitation energies have greater differences with experimental values. To optimize the local central potential, which should reflect the polarization of the frame containing the exchange member, the following one-electron configurations were used $4p^6nl$ (n=5, 6, 7, l=0, 1, 2, 3). To account for correlation effects (BK) the following configurations were used $4p^6nl$ (n=5, 6, 7, l=0, 1, 2, 3), $4p^5nln'l'$ (nl=5s, 6s, 5p, 4d, 5d, $n'l'$=5s, 6s, 5p, 6p, 4d, 5D, 4f, 5f, 5G) for the main $4p^65s$ state of the Rb Atom and for $4p^6$, $4p^5nl$ (nl=5s, 6s), $4p^4nln'l'$ (nl=5s, 5p, $n'l'$=5s, 5p, 4D, 5D) the final state of Rb+. Calculations were performed in *jj* connections.

Results and Discussion

In Figure 1 presented a comparison of experimental excitation cross-sections [5] of doublet $(4p^55s2)^2P_{3/2,1/2}$ AIC with our theoretical calculations and data [9]. The experimental data were normalized to our RCX calculations at a collision energy of 650 eV. In the region of energies above 100 eV, our theoretical excitation cross-sections of PCX and PCX-BK $(4p^55s^2)^2P_{1/2,3/2}$ states within the experimental error satisfactorily describe the experimental data. Born and PCX excitation cross-sections [9] in this energy range underestimate the absolute values of the cross-sections. However, it should be noted that both our data and the data [9] correspond to the rule of the ratio of cross-section values $^2P_{3/2}$:$^2P_{1/2}$≈2:1 [14]. Why is it correct to normalize for our data for comparison, and not for data [9]? According to the data [8], and the R-matrix method is the most accurate method for calculating cross-sections in the near-threshold energy range, the excitation cross-sections should have even higher absolute values of effective cross-sections, i.e. our data are closer to them. In this figure, comparison with them is not given, since the excitation cross-sections $(4p^55s^2)^2P_{1/2,3/2}$ states in [8] are represented in a very narrow range of 15-20 eV.

A significant difference between experiment and theory exists for small and medium values of collision energy. Worth noting that the description of processes in the range of energies of 20-90 EV is an issue for all existing theoretical approximations, since it requires simultaneous consideration of a large number of high-energy configurations as $4p^6$ shell and excitation from the deeper shells of the rubidium atom. It is also necessary to take into account the contribution of possible cascade and radiation transitions, which is a very complex theoretical problem. Indeed, as the analysis of the experimental cross-section of the excitation state $(4p^55s^2)^2P_{1/2}$ shows, at collision energies of 18-30 eV, oscillatory behaviour and an increase in the cross-section value of up to 20% are observed. As follows from [15] in the wavelength range from 624 to 577 Å (19.8-21.5 eV), the photoabsorption

spectrum of the $4p^6$ shell contains a total of 46 lines, of which only 8 have an extended autoionization profile. This means that most AIC located above 19 eV decay mainly due to radiation transitions to low-energy AIC, in particular $(4p^55s^2)^2P_{1/2}$. Regarding the cross-section of the excitation state $(4p^55s^2)^2P_{3/2}$, then in the energy range of 20-30 EV, the noticeable effect of cascading population processes from high-energy levels is not observed. The PCX-BR approximation best describes the excitation process in this region. The figure shows that in the near-threshold region of collision energies, the experimental data of both levels have a distinct resonant character. The size of the cross-sections of the latter exceeds the efficiency of the direct process by almost one and a half times. Detailed analysis of this section in [8] showed that all resonances here are Feshbach-type resonances with a common 4p configuration $^5 6s^5p^2$ in the case of $(4p^55s^2)^2P_{3/2}$ and a common configuration $4p^55s4d6s$ for autoionization state $(4p^55s^2)^2P_{1/2}$. Theoretical approximations of PCX and Born in the near-threshold region of collision energies cannot qualitatively describe such resonant processes.

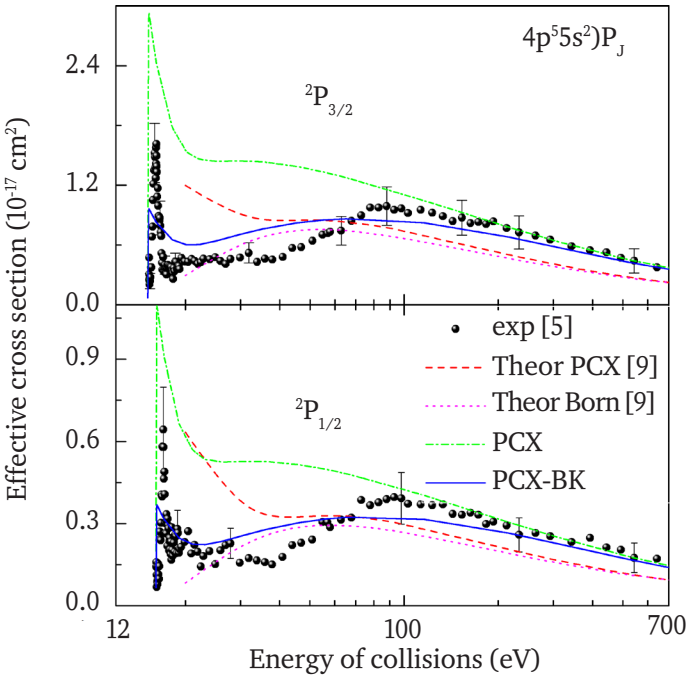

Figure 1. Effective cross-sections of doublet excitation $(4p^55s^2)^2P_{3/2,1/2}$ AIC of the rubidium atom

The cross-section of the PCX without taking into account configuration mixing significantly overestimates the efficiency of near-threshold excitation, but still assumes its presence, as well as the approximation of the PCX [9]. The calculations performed in [9] in the Born approximation do not take into account the possibility of resonant excitation, as evidenced by the behaviour of the corresponding excitation cross-section in the near-threshold region of collision energies. Since the Born approximation is a scattering in a potential field, it does not describe the details of the scattering process at low collision energies. Although the PCX-BK approximation differs from the experimental data in the near-threshold region, it also predicts a sharp increase in the efficiency of resonant excitation of AIC data. This indicates that the method takes into account to a greater extent the perturbations of the incoming and scattered waves by the field of the atomic residue and, at the excitation threshold, provides for the possibility of capturing the incoming electron in the discrete spectrum state with simultaneous excitation of the bound electron from the inner shell.

In our research, the ratio parameter

$R_0 = {}_{\sigma 3/2/\sigma 1/2}$ of line intensities $(4p^5 5s^2)^2P_{3/2}$ and $(4p^5 5s^2)^2P_{1/2}$, which according to [14] should be correlated as 2: 1 or 100% to 50% is also studied. In Figure 2 experimental data are compared with theoretical calculations in the Born approximation, PCX and relativistic approximation of distorted waves with exchange (PCXO) [9]. The general behavior of the dependence of the ratio of experimental line intensities is characterized by a sharp near-threshold resonance, an oscillatory structure up to 30 eV, and then an almost linear classical dependence up to 650 eV. This behaviour is primarily due to the dominant role of negative ion States in the near-threshold excitation of AIC $(4p^5 5s^2)^2P_{3/2,1/2}$, and the influence of cascade population at energies up to 30 eV, which has already been discussed above. Theoretical calculations of PCX and Born in the region of collision energies up to 30 eV, as already shown in the description of excitation cross-sections, differ significantly. It is difficult to talk about the quality of theoretical values of the ratio parameter R_0 in this area since the experimental data also have a large spread of values, but as can be seen, there is a perfect coincidence of our theoretical calculations of the RCX with the RCX data [9], both with and without exchange. Nevertheless it is necessary to note the remarkable coincidence of theoretical and experimental data in the region of collision energies of 35-650 eV. This means that in the case of theoretical calculations of the PCX in the strong coupling decomposition, configurations are successfully selected that take into account the correlation mixing of levels and the correctly selected model potential used to determine single-electron radial wave functions. Also, such a good agreement shows the reliability of experimental measurements.

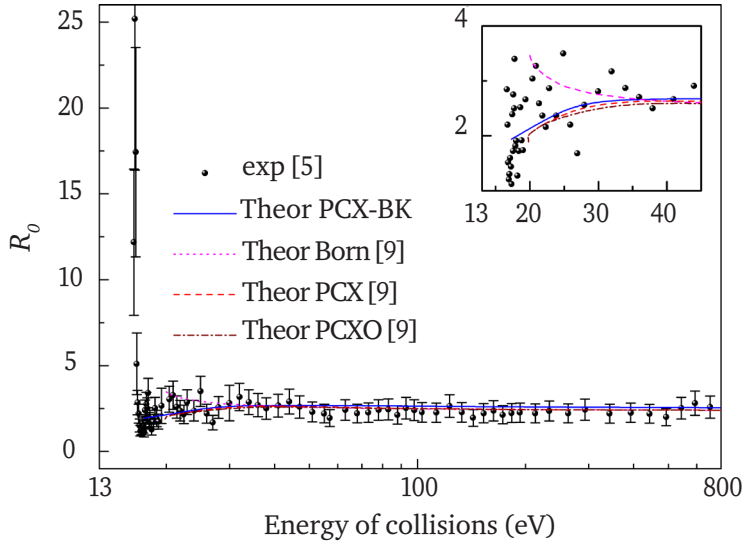

Figure 2. Intensity ratio $R_0 = \sigma_{zb}[(4p^5 5s^2)^2P_{3/2}]/\sigma_{zb}[(4p^5 5s^2)^2P_{1/2}]$ AIC of the rubidium atom

Figure 3 shows the experimental excitation cross-sections [6] of the lowest quartets $(4p^5 4d5s)^4P_{1/2,3/2,5/2}$ AIC in comparison with our theoretical calculations of PCX-BK in the range of collision energies of 16-700 eV and R-matrix with B-splines data [8] (16-50 eV).

Experimental data are normalized to PCX-BK data at a collision energy of 350 eV for states $^4P_{3/2,5/2}$ and 110 eV for $^4P_{1/2}$. It should be noted that in the case of quartet AIC, the PCX method without correlation corrections gave unsatisfactory results, which were rejected. This indicates the complexity of the process of excitation and decay of these states, as well as the fact that configuration mixing plays a more significant role here. The general view of all experimental cross-sections is broadly similar and reflects the exchange nature of excitation of these quartet levels. Although theoretical data differ significantly in general behavior, but in absolute terms correlate well with each other when describing experimental data. Both types of theoretical data do not

contradict the rule of correlation of the intensity of spectral lines within the same series $^4P_{5/2}$:$^4P_{3/2}$:$^4P_{1/2}$≈3:2:1 [14]. All functions start with intense narrow maxima (ΔE<1 eV), which are located just beyond the excitation threshold, indicating the presence of effective resonant excitation in the near-threshold energy region, as indicated by studies [8] and our theoretical calculations. In the energy range of 17-24 eV, a slight increase in the excitation efficiency is noticeable at all cross-sections, which is most clearly manifested for the level of $^4P_{1/2}$.

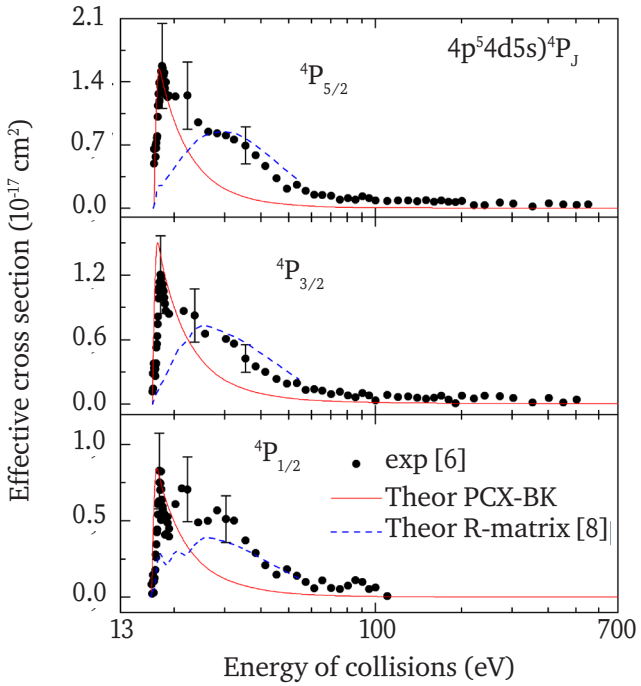

Figure 3. Effective quartet excitation cross-sections $(4p^54d5s)^4P_{1/2,3/2,5/2}$ AIC of the rubidium atom

This increase in cross-section has a cascading origin due to the radiation decay of high-energy states. If our theoretical calculations in this region significantly underestimate the values of all excitation cross-sections, then the data [8] perfectly predict an increase in the cross-section size due to the presence of additional input as a result of radiation decay from the upper 4p levels ^{5}4d5s, 4p^{5}5s5p, 4p^{5}5p^2, 4p^{5}4d5p configurations. The disadvantage of our theoretical calculations is precisely the impossibility to take into account cascade transitions, a very difficult theoretical problem indeed. In the region of collision energies above 70 eV, our theoretical PCX-BK data qualitatively describe the excitation process of quartet AIC data, which allows us to normalize experimental data in order to obtain absolute values of effective excitation cross-sections $(4p^54d5s)^4P_{1/2,3/2,5/2}$ AIC of the rubidium atom. The excitation energies and absolute values of the experimental excitation cross-sections obtained during normalization for our theoretical calculations of PCX-BK are shown in Table 1.

Table 1. Figure 1: Calculated and experimental electron excitation energies (E_{zb}, eV), excitation cross-sections (σ, 10^{-17} cm^2) in maxima σ_{max} and at collision energies of 100 and 500 eV, as well as the probability of electron decay (A, c^{-1}) AIS $4p^5nl(L_1S_1)n'l'LSJ$ the rubidium atom

$(L_1S_1)LSJ$	E_{zb}, calculation	E_{zb}, experiment [12]	σ, 10^{-17} см^2			A, c^{-1}
			σ_{max}	≈ 100 eV	≈ 500 eV	
$5s^2\ ^2P_{3/2}$	15.134	15.31	1.61	0.92	0.47	$7.65\cdot10^{12}$
$5s^2\ ^2P_{1/2}$	16.040	16.16	0.64	0.37	0.20	$1.04\cdot10^{13}$
$4d(^3P)5s\ ^4P_{1/2}$	16.665	16.69	0.08	0.06	0	$9.08\cdot10^{8}$
$4d(^3P)5s\ ^4P_{3/2}$	16.754	16.79	1.21	0.08	0.04	$6.12\cdot10^{7}$
$4d(^3P)5s\ ^4P_{5/2}$	16.907	16.97	1.57	0.08	0.03	$5.31\cdot10^{11}$

Conclusions

The study presents a comparison of experimental cross-sections of doublet excitation $(4p^55s^2)^2P_{3/2,1/2}$ and quartet $(4p^54d5s)^4P_{1/2,3/2,5/2}$ autoionization states with available theoretical data and our relativistic calculations. The results of the study of the parameter R_0 of the intensity ratio for the states $^2P_{3/2}$ and $^2P_{1/2}$ configuration $4p^55s^2$ are presented. It is shown that in the region of energies above 70 eV, our calculations in the approximation of distorted waves well describe the experimental data. At low collision energies, our calculations qualitatively predict the presence of near-threshold resonant excitation, and in the tange of average energies of 20-50 EV, only the R-matrix method qualitatively describes the complex nature of excitation and decay of the lowest quartet autoionization states of the rubidium atom. A comprehensive analysis of the obtained results with the involvement of available experimental and theoretical data showed that the approximation of relativistic distorted waves, taking into account configuration mixing, is a successful tool for describing the autoionization states of a rubidium atom in a wide range of collision energies and allowed us to obtain absolute values of excitation experimental cross-sections of $(4p^55s^2)^2P_{3/2,1/2}$ and $(4p^54d5s)^4P_{1/2,3/2,5/2}$ states.

The study is supported by the scientific project of young scientists of the National Academy of Sciences of Ukraine “Dynamics of Formation of Excited States of Atoms and Ions in Plasma on Metal Pairs: Mechanisms of Elementary Processes”.

References

[1] Borovik A. Excitation-autoionization cross section of alkali atoms by electron impact. *J. Phys. B: At. Mol. Opt. Phys.* 2013;(46):215201.

[2] Evrij MJ, Borovik O, Shimon LL, Kontros JE. Resonance excitation of the $3p^6$-subshell in potassium: Contribution to the single ionization. *Nucl. Instr. Meth. Phys. Res. B.* 2005;(233):280-83.

[3] Borovik A, Roman V, Kupliauskiene A. The autoionization cross section of rubidium atoms excited by electron impact. *Reports of NASU.* 2013;(3):58-64.

[4] Borovik A, Kupliauskiene A. The $5p^6$ autoionization cross section of cesium atoms: Contribution t single ionization by electron impact. *J. Phys. B: Atom. Mol. Opt. Phys.* 2009;42(16):165202.

[5] Borovik A, Ilyashevytch V, Kupliauskiene A. Ejected-electron excitation functions of the $(4p^55s^2)^2P_{3/2,1/2}$ autoionizing states of rubidium atoms excited by 15 to 640 eV electrons. *J. Phys. Conf. Ser.* 2012;(388):042007.

[6] Roman V, Tymchyk R, Kupliauskiene A, Borovik A. Electron-impact excitation of the $(4p^54d5s)4PJ$ autoionizing states in Rb atoms. Gothenburg; 2012; 163 p.

[7] Borovik A. Resonance excitation of autoionizing states in alkali atoms by electron impact. *Scientific Herald of Uzhhorod University. Series “Physics”.* 2013;(34):173-81.

[8] Borovik A, Roman V, Zatsarinny O, Bartschat K. Electron impact excitation of the lowest doublet and quartet core-excited autoionizing states in Rb atoms. *J. Phys. B: At. Mol. Opt. Phys.* 2013;46(1):015203-209.

[9] Kaur S, Srivastava R. Excitation of the lowest autoionizing $np^5(n+1)s^2$, $^2P3/2, 1/2$ states of Na (n=2), and Cs (n=5) by electron impact. *J. Phys. B: At. Mol. Opt. Phys.* 1999;32(10):2323-42.

[10] Gu MF. The flexible atomic code. *Can. J. Phys.* 2008;(86):675-689.

[11] Kupliauskiene A, Kerevicius G. Theoretical study of the $4pp^5nln'l'$ autoionizing states of Rb excited by electron impact. *Phys. Scr.* 2013;(88):065312-319.

[12] Borovik A, Roman V, Kupliauskiene A. The $4p^6$ autoionization cross section of Rb atoms excited by low-energy electron impact. *J. Phys. B.* 2012;45(4):045204-214.

[13] Roman V, Kupliauskiene A, Borovik A. Excitation and ionization of outer shells in Rb by electron impact. *J. Phys. B.* 2015(48):205204-209.

[14] Frisch SE. Optical spectra of atoms. Moscow; 1968. 640 p.

[15] Shender IO, Pogodin AI, Bereznyuk SM, Filep MY, Kokhan OP, Studenyak IP. Influence of the cation substitution upon the electrical conductivity of the superionic ceramics on the basis of microcrystalline powders of $(Cu_{1-x}Ag_x)_7SiS_5I$. *Sci. Herald Uzhhorod Univ. Ser. "Physics"*, 2020;47:21-31.

Список використаної літератури

[1] Borovik A. Excitation-autoionization cross section of alkali atoms by electron impact. *J. Phys. B: At. Mol. Opt. Phys.* 2013;(46):215201.

[2] Evrij MJ, Borovik O, Shimon LL, Kontros JE. Resonance excitation of the $3p^6$-subshell in potassium: Contribution to the single ionization. *Nucl. Instr. Meth. Phys. Res. B.* 2005;(233):280–83.

[3] Borovik A, Roman V, Kupliauskiene A. The autoionization cross section of rubidium atoms excited by electron impact. *Reports of NASU.* 2013;(3):58–64.

[4] Borovik A, Kupliauskiene A. The $5p^6$ autoionization cross section of cesium atoms: Contribution t single ionization by electron impact. *J. Phys. B: Atom. Mol. Opt. Phys.* 2009;42(16):165202.

[5] Borovik A, Ilyashevytch V, Kupliauskiene A. Ejected-electron excitation functions of the $(4p^55s^2)^2P_{3/2,1/2}$ autoionizing states of rubidium atoms excited by 15 to 640 eV electrons. *J. Phys. Conf. Ser.* 2012;(388):042007.

[6] Roman V, Tymchyk R, Kupliauskiene A, Borovik A. Electron-impact excitation of the $(4p^554d5s)4PJ$ autoionizing states in Rb atoms. Gothenburg; 2012; 163 p.

[7] Borovik A. Resonance excitation of autoionizing states in alkali atoms by electron impact. *Scientific Herald of Uzhhorod University. Series "Physics".* 2013;(34):173–81.

[8] Borovik A, Roman V, Zatsarinny O, Bartschat K. Electron impact excitation of the lowest doublet and quartet core-excited autoionizing states in Rb atoms. *J. Phys. B: At. Mol. Opt. Phys.* 2013;46(1):015203.

[9] Kaur S, Srivastava R. Excitation of the lowest autoionizing $np^5(n+1)s^2$, $^2P3/2$, 1/2 states of Na (n=2), and Cs (n=5) by electron impact. *J. Phys. B: At. Mol. Opt. Phys.* 1999;32(10):2323–42.

[10] Gu MF. The flexible atomic code. *Can. J. Phys.* 2008;(86):675–689.

[11] Kupliauskiene A, Kerevicius G. Theoretical study of the $4pp^5nln'l'$ autoionizing states of Rb excited by electron impact. *Phys. Scr.* 2013;(88):065312–319.

[12] Borovik A, Roman V, Kupliauskiene A. The $4p^6$ autoionization cross section of Rb atoms excited by low-energy electron impact. *J. Phys. B.* 2012;45(4):045204–214.

[13] Roman V, Kupliauskiene A, Borovik A. Excitation and ionization of outer shells in Rb by electron impact. *J. Phys. B.* 2015(48):205204–209.

[14] Frisch SE. Optical spectra of atoms. Moscow; 1968. 640 p.

[15] Shender IO, Pogodin AI, Bereznyuk SM, Filep MY, Kokhan OP, Studenyak IP. Influence of the cation substitution upon the electrical conductivity of the superionic ceramics on the basis of microcrystalline powders of $(Cu_{1-x}Agx)_7SiS_5I$. *Sci. Herald Uzhhorod Univ. Ser. "Physics",* 2020;47:21-31.

Теоретичні розрахунки електронного збудження найнижчих автоіонізаційних станів атома Rb

В.І. Роман, О.М. Поп, І.В. Пилипчинець

Інститут електронної фізики НАН України
88000, вул. Університетська, 21, м. Ужгород, Україна

Анотація

Мета. Значення перерізу автоіонізації та його енергетична залежність значною мірою визначаються збудженням та подальшим розпадом електронів найнижчих енергетичних станів. Нещодавно було отримано експериментальні дані про перерізи збудження найнижчого дублету атома рубідію $(4p^55s^2)^2P_{3/2,1/2}$ та квартету $(4p^54d5s)^4P_{1/2,3/2,5/2}$ автоіонізаційних станів, що сприяло їх теоретичним дослідженням.

Методи. Теоретичні розрахунки було проведено за допомогою універсального пакету програм «Гнучкий атомний код», який враховує релятивістську природу збудження складних атомів за допомогою гамільтоніана Дірака-Кулона. Радіальні орбіталі для основних релятивістських хвильових функцій було отримано шляхом розв'язання рівняння Дірака-Фока-Слейтера.

Результати. Подано порівняння експериментальних перерізів збудження для дублетних $(4p^5 5s^2)^2P_{3/2,1/2}$ та квартетних $(4p^5 4d5s)^4P_{1/2,3/2,5/2}$ автоіонізаційних станів з наявними теоретичними даними та нашими релятивістськими розрахунками. Представлено результати дослідження параметра R_0 відношення інтенсивностей для станів $^2P_{3/2}$ та $^2P_{1/2}$ конфігурації $4p^5 5s^2$. Показано, що наші розрахунки в наближенні спотворених хвиль добре описують експериментальні дані в області енергії вище 70 еВ. При малих енергіях зіткнення наші розрахунки якісно передбачають наявність порогового резонансного збудження; однак у енергетичній області 20–50 еВ лише метод R-матриці якісно описує складну природу збудження та розпаду найнижчих квартетних автоіонізаційних станів атома рубідію.

Висновки. Електронне збудження дублету $(4p^5 5s^2)^2P_{3/2,1/2}$ та квартету $(4p^5 4d5s)^4P_{1/2,3/2,5/2}$ автоіонізуючих станів атома рубідію в діапазоні енергій зіткнення від порогів збудження до 700 еВ було досліджено в термінах релятивістського наближення спотворених хвиль. Комплексний аналіз отриманих результатів з використанням наявних експериментальних та теоретичних даних показав, що апроксимація релятивістських спотворених хвиль з урахуванням конфігураційного змішування є відповідним інструментом для опису автоіонізаційних станів атома рубідію у широкому діапазоні енергій зіткнення. для отримання абсолютних значень експериментальних перерізів збудження

Ключові слова: атом, електронне збудження, автоіонізаційні стани, переріз збудження

Теоретические расчеты электронного возбуждения низких автоионизационных состояний атома Rb

В.И. Роман, О.М. Поп, И.В. Пилипчинец

Институт электронной физики НАНУ, Украина
88000, ул. Университетская, 21, г. Ужгород, Украина

Аннотация

Цель. Значения сечения автоионизации и их энергетическая зависимость в значительной степени определяются возбуждением и последующим распадом электронов самых низких энергетических состояний. Недавно были получены экспериментальные данные о сечениях возбуждения самого низкого дублета атома рубидия $(4p^5 5s^2)^2P_{3/2,1/2}$ и квартета $(4p^5 4d5s)^4P_{1/2,3/2,5/2}$ автоионизационных состояний, что способствовало их теоретическим исследованиям.

Методы. Теоретические расчеты были произведены с помощью универсального пакета программ «Гибкий атомный код», учитывающего релятивистскую природу возбуждения сложных атомов с помощью гамильтониана Дирака-Кулона. Радиальные орбитали для основных релятивистских волновых функций были получены решением уравнения Дирака-Фока-Слейтера.

Результаты. Представлено сравнение экспериментальных сечений возбуждения для дублетных $(4p^5 5s^2)^2P_{3/2,1/2}$ и квартетных $(4p^5 4d5s)^4P_{1/2,3/2,5/2}$ автоионизационных состояний с имеющимися теоретическими данными и нашими релятивистскими расчетами. Представлены результаты исследования параметра R_0 относительно интенсивностей для состояний $^2P_{3/2}$ и $^2P_{1/2}$ конфигурации $4p^5 5s^2$. Показано, что наши расчеты в приближении искаженных волн хорошо описывают экспериментальные данные в области энергии выше 70 эВ. При малых энергиях столкновения наши расчеты отменно подразумевают наличие порогового резонансного возбуждения; однако в энергетической области 20–50 эВ только метод R-матрицы качественно описывает сложную природу возбуждения и распада самых низких квартетных автоионизационных состояний атома рубидия.

Выводы. Электронное возбуждение дублета $(4p^5 5s^2)^2P_{3/2,1/2}$ и квартета $(4p^5 4d5s)^4P_{1/2,3/2,5/2}$ автоионизирующих состояний атома рубидия в диапазоне энергий столкновения от порогов возбуждения до 700 эВ волн. Комплексный анализ полученных результатов с использованием имеющихся экспериментальных и теоретических данных показал, что аппроксимация искаженных релятивистских волн с учетом конфигурационного смешения является соответствующим инструментом для описания автоионизационных состояний атома рубидия в широком диапазоне энергий столкновения для получения абсолютных значений экспериментальных сечений возбуждения

Ключевые слова: атом, электронное возбуждение, автоионизационные состояния, сечение возбуждения

Scientific Herald of Uzhhorod University
Series "Physics"

Journal homepage: https://physics.uz.ua/en
Issue 48, 67-77
Received: 29.08.2020. Revised: 15.09.2020. Accepted: 20.11.2020

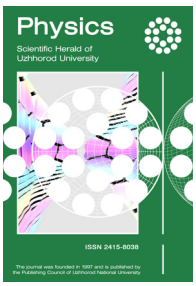

UDC 539.1.08, 539.198
PACS 31.10.+z; 31.15.−p; 34.10.+x; 34.35.+a; 34.80.−i
DOI: 10.24144/2415-8038.2020.48.67-77

Calculations of the Energy Structure of P, S Atoms by the R-Matrix Method with B-Splines

I.I. Nebola*, A.F. Katanytsia, A.Ya. Shteyfan, V.I. Sidey, I.P. Studenyak

Uzhhorod National University
88000, 54 Voloshyn Str., Uzhhorod, Ukraine

Abstract

Purpose. Over the past decades, the physics of electron-atomic (EA) collisions has been intensively developed. This is due both to the fundamental nature of the studied processes and applied needs. This is primarily about understanding at a deep level the behavior of submicroscopic, often strongly correlated, quantum mechanical many-particle systems. The result of this understanding is obtaining a large amount of data necessary for modeling the behavior of various types of plasma and discharges, as well as to diagnose their properties.

Methods. We have presented the general principles and idea, underlying in the B-spline R-matrix method (BSR) with a non-orthogonal orbitals. The use of non-orthogonal single-electron orbitals eliminates orthogonal restrictions applied in many other theoretical approaches. These restrictions are introduced purely for the convenience of calculation, rather than for reasons of physical necessity. Rejecting the orthogonality conditions, BSR method significantly improves the accuracy of the target description. Accordingly, it becomes possible to further accurate calculation of the collision processes.

Results. We considered the application of the BSR method to the calculation of the energy structure of a phosphorus and sulfur atoms, that is of considerable practical interest. The calculation results demonstrate good agreement with the available experimental data.

Conclusions. In this paper, the energy structure of the phosphorus atom was calculated. The calculation results demonstrate good agreement with the available experimental data. In the future, our data will be used in the study of electron scattering on phosphorus and sulfur atoms.

Keywords: phosphorus atom, sulfur atom, structure calculation of atomic systems, *B*-spline *R*-matrix method, Hartree-Fock method, multi-electronic bases, correlation interaction, single- and multi-configuration approximation

Suggested Citation:
Nebola II, Katanytsia AF, Shteyfan AYa, Sidey VI, Studenyak IP. Calculations of the energy structure of P, S Atoms by the R-matrix method with B-splines. *Scientific Herald of Uzhhorod University. Series "Physics"*. 2020;(48):67-77.

*Corresponding author

Introduction

In recent decades, there has been an intensive development in the study of electron-atom (EA) collision processes. The importance of the results of systematic calculations of the structural properties of phosphorus and sulphur atoms for various applications in atomic physics, electron-atom collision theory, and plasma modeling cannot be overemphasized. Thus, elementary processes involving atoms and ions play an important role in plasma injection and diagnostics in modern thermonuclear installations and affect the processes occurring in the plasma itself, determine the operating conditions of X-ray and gas lasers, and are important in the design and use of heavy ion accelerators.

In this research, the energy structure of phosphorus and sulphur atoms is calculated using the method proposed in [3-11] *R*-matrix with non-orthogonal orbitals and *B*-splines as basic functions (BSR) [1]. In the calculations of the energy structure of P, S atoms, the multiconfiguration Hartree-Fock method (MCHF) [2] with non-orthogonal orbitals optimized in independent calculations for individual terms was also used. The results obtained will be used in the future to study the processes of scattering slow electrons on phosphorus and sulphur atoms.

Calculation Methods

In this section, we will briefly look at the main aspects of the new version of the *B*-spline *R*-matrix method (BSR Method) [1]. This method is successfully applied both in calculations of the atomic structure and in the study of the processes of elastic and inelastic scattering of slow electrons on complex atoms and ions. A special feature of the BSR method is the use of basic splines B_i to represent both the bound orbitals of the target atom and the orbitals of the scattered electron. The problem of low-energy electron scattering on N-electron atom is reduced to solving the Schrödinger equation (1):

$$(H_{N+1} - E)\psi_\alpha^G(X, x_{N+1}) = 0,$$
$$H_{N+1} = \sum_{i=1}^{N+1}\left(-\frac{1}{2}\nabla_i^2 - \frac{Z}{r_i}\right) + \sum_{i>j=1}^{N+1}\frac{1}{r_{ij}} \quad (1)$$

with appropriate boundary conditions. Here E and H_{N+1} – full energy and Hamiltonian $(N+1)$-electronic system "atom + incident electron", Z – nuclear charge. Hamiltonian H_{N+1}(1) diagonal to the total orbital momentum L, full spin S, their projections M_L, M_S on a given axis and π parity. Function $\Psi_\alpha^G(X,x_{N+1})$ commonly referred to as the wave function collapse is a completely antisymmetric wave function of $(N+1)$-electron system, $X\equiv(x_1, \ldots, x_N)$, $G\equiv(\gamma LSM_L M_{S\pi})$, a $x_i\equiv(\vec{r_i}, \sigma_i)$ denotes a set of spatial $\vec{r_i}$ and spin σ_i coordinates of i electron. The index α characterizes the initial conditions and usually denotes the input channel $e+A$ – scattering. Excluding ionization decomposition of the total wave function collapse $\Psi_\alpha^G(X,x_{N+1})$ can be represented as (2):

$$\Psi_\alpha^G(X, x_{N+1}) = A\sum_{i=1}^{n}\bar{F}_i^G(X;\ \hat{r}_{N+1}, \sigma_{N+1}) \times \frac{F_{i\alpha}^G(r_{N+1})}{r_{N+1}} + \sum_{j=1}^{m} c_j\chi_j^G(X, x_{N+1}) \quad (2)$$

Here A is the antisymeterization operator; $\bar{F}_i^G$ – wave function of i- channel built by vector relation of the wave function N-electron target $F_i(X)$ with the angular and spin parts of the wave function of the scattered electron; $\chi_i^G(X,x_{N+1})$ – a set of quadratically integrated antisymmetric correlation functions that provide completeness of decomposition (2). The problem is to find radial wave functions of $F_{i\alpha}^G(r_{N+1})$ scattered electron and coefficients cj of decomposition (2). Atomic wave functions $F_i(X)$ are plotted as a multi-configuration schedule (3):

$$F_i(x_1, \ldots, x_N) = \sum_j c_{ij}\varphi_j(x_1, \ldots, x_N) \quad (3)$$

where φ_j – single-configuration wave functions of the target atom. Coefficients c_{ij} obtained by diagonalization of N- electronic Hamiltonian of HN target atom (4):

$$\langle F_i | H_N | \Phi_j \rangle = E_i(Z, N)\delta_{ij} \quad (4)$$

Usually, the first sum on the right side of decomposition (2) includes only those target states that, at a given energy $E = E_i + \frac{k_i^2}{2}$ correspond to the so-called open channels. In the first sum can also be included some pseudostates which approximately represent states of a continuous spectrum. The selection of pseudostates is carried out on the basis of accurate account of the polarizability of the main and several excited states of the target. In addition to using pseudostates, the contribution of closed channels can be partially accounted for using a finite number of correlation functions $\chi_i^G(X,x_{N+1})$ included in the second sum of the decomposition (2).

Basic functions φ_j and χ_j in decompositions (2), (3) are constructed from single-electron atomic orbitals $\varphi_{\alpha i}$, which in the approximation of the central field have the form (5):

$$\varphi_{\alpha_i}(x) = 1/r \cdot P_{n_i l_i}(r) Y_{l_i m_i}(\hat{r}) \chi(m_s|\sigma), x \equiv (\vec{r_i}, \sigma) \quad (5)$$

where α_i – abbreviated designation of a set of quantum numbers n_i, l_i, m_i and mS. In the standard version *R*-matrix approach for easy calculation of radial wave functions of a scattered electron $F_{i\alpha}^G$ are selected orthogonal to all atomic orbitals of the target $P_{nj\,lj}$ of the same symmetry (6):

$$\int_0^\infty P_{n_j l_j}(r) F_{i\alpha}^{\mathrm{G}}(r) dr = 0 \quad (6)$$

when $l_j = l_i$.

Condition (6) actually means that an incident electron cannot be virtually trapped in one of the unfilled sub-shells taken into account in decomposition (3) of the target states. Substituting decomposition (2) into equation (1), multiplying it alternately by the functions $\bar{F}_i^G$ and $\bar{\chi}_j^G$ after integration over all variables except r_{N+1}, can be obtained a system of integrodifferential equations for functions $F_i \equiv F_{i\alpha}$ (7):

$$\left(\frac{d^2}{dr^2} - \frac{l_i(l_i+1)}{r^2} + \frac{2Z}{r} + k_i^2\right) F_i(r) = 2\sum_j (V_{ij} + W_{ij} + X_{ij}) F_j(r) \quad (7)$$

where $k_i^2 = 2[E - E_i(Z,N)]$, a V_{ij}, W_{ij}, X_{ij} – local direct, non-local exchange, and non-local correlation potentials, respectively. For electron scattering on complex atoms, an explicit form of these potentials is generated automatically by the BSR program [1], depending on the type of input data.

To solve the CC equation system (7), can be applied a variant of the method *R*-matrix based on the use of non-orthogonal orbitals and *B*-splines as basic functions. This method makes it possible to describe various types of reactions within a single formalism, such as elastic scattering, excitation, and ionization of an atom by electron shock. Main idea *R*-matrix method consists in dividing the configuration space of the "atom + electron" system into two regions: internal $r<A$ and external $r>a$. The radius of the inner region $r=A$ is chosen so that the exchange and correlation effects are sufficiently small at $r \geq a$. The full wave function $(N+1)$ of an electronic system in the inner region can be represented at a given energy E as a decomposition:

$$\Psi_{\mathrm{E}}^{\mathrm{G}} = \sum_k A_{Ek}^{\mathrm{G}} \Psi_k^{\mathrm{G}} \quad (8)$$

by an energy independent discrete base set Ψ_k^G

$$\Psi_k^G(X, x_{N+1}) = A \sum_{ij} \bar{F}_i^G(X; \hat{r}_{N+1}, \sigma_{N+1}) \times \frac{u_j(r_{N+1})}{r_{N+1}} c_{ijk}^G + \sum \chi_i^G(X, x_{N+1}) d_{ik}^G \quad (9)$$

where $\bar{F}_i^G$ and $\bar{\chi}_i^G$ are defined in the same way as in formula (2). Functions $F_{i\alpha}^G$, describing the radial motion of a scattered electron in i-channel, are presented as a linear combination of a finite number of basis functions uj, which satisfy the boundary conditions $u_j = 0, (a/u_j) du_j/dr|_{r=a} = b$, where b – an arbitrary valid constant. For such basic functions, the Hamiltonian (1) in the inner domain is not Hermitian due to nonzero (at $r=a$) surface terms arising from the kinetic energy operator. However, these terms can be removed using the Bloch operator L_{N+1}. The formal solution of Schrödinger's Equation (1) takes the following form (10):

$$|\Psi\rangle = \frac{1}{2}\sum_{kj}|\Psi_k^{\mathrm{G}}\rangle\langle\Psi_k^{\mathrm{G}}|\overline{\mathrm{F}_j^{\mathrm{G}}}\rangle(E_k - E)^{-1} \times (\frac{d}{dr_{N+1}} - \frac{b_j}{r_{N+1}})\langle\overline{\mathrm{F}_j^{\mathrm{G}}}\,|\Psi\rangle \quad (10)$$

Projecting this equation onto channel functions $\bar{F}_i^G$ and performing calculations on the border of the inner region, the following results are obtained (11):

$$F_i^{\mathrm{G}}(a) = \sum_{j=1}^{n} R_{ij}^{\mathrm{G}}(E)(\frac{adF_i^{\mathrm{G}}}{dr_{N+1}} - b_j F_j^{\mathrm{G}})_{r_{N+1}=a} \quad (11)$$

where entered R- a matrix is introduced with elements (12):

$$R_{ij}^{\mathrm{G}}(E) = \frac{1}{2a}\sum_k \frac{w_{ik}^{\mathrm{G}}(a)w_{jk}^{\mathrm{G}}(a)}{(E_k^{\mathrm{G}} - E)} \quad (12)$$

radial functions F_i^G and surface amplitudes w_{ik}^G are given. Diagonalizing the matrix $\langle\psi_k^{\mathrm{G}}|H_{N+1} + + L_{N+1}|\psi_k^{\mathrm{G}}\rangle_{int}$ for each set of quantum numbers G, the energies E_k^G and coefficients c_{ijk}^G, d_{ik}^G in decomposition can determined (9), i.e. wave functions ψ_k for the corresponding base states. However, it only needs to be done once to determine R-matrix over the entire range of collision energies.

As noted above, the inclusion in the output decomposition (9) of additional correlation functions χ_j^G allows to partially take into account the effects associated with the conditions of orthogonality (6) of the functions $F_{i\alpha}^G$ and the limitation of the first sum in (9) finite number of terms. However, this leads in most cases to the appearance of a pseudo-resonant structure in the scattering cross-sections and to an excessively large number of additional integro-differential equations, which must be left out in (9) for realistic calculations of complex atoms and the processes of their interaction with electrons. In this respect, it is worth mentioning that condition (6) is not mandatory and does not follow from general quantum mechanical principles. Therefore, in studies [3-11], the authors abandoned the requirement (6) of orthogonality of functions $F_{i\alpha}^G(r_{N+1})$ to bound orbitals P_{njlj} of targets of the same symmetry. Worth noting that in BSR version of the R-Matrix method proposed by us, correlation functions χ_j can be left out, or used only to compensate for defects in the collapse function associated with limiting the first sum in decomposition (9) by a finite number of terms $\psi_{E^*}^G$.

Calculation Results

A) Energy Structure of the P Atom

Structural calculations in the case of the *P* atom were performed using both the MCHF package [2] and the BSR package [1]. By the BSR Method [1] in LS- approximation calculated single-electron orbitals of 36 lower states of the *P* atom with configurations $1s^22s^22p^63s^23p^3(^4S^o, ^2D^o, ^2P^o)$, $3s^23p^2$ (^3P) nl (n=3, 4, 5, 6; l=0, 1, 2), $3s^23p^2$ (^1D) nl (n=4; l=0, 1), $3s^23p^2$ (^1P) 4s and $3s3p^4(^4P, ^2D, ^2S)$. The spectrum of the phosphorus atom according to NIST data [12] is quite complex. The energy values of the spectroscopic states of the *P* atom are obtained by weight averaging of the fine structure levels during the transition from *LSJ-NIST* representation of the approximation *LS*-coupling used. The next few levels of the *P* spectrum are formed mainly by the excitation of one 3*p*-electron from the valence shell at one of the spectroscopic levels of configuration $3s^23p^2$ (^3P) nl (n=3, 4, 5, 6, 7; l=0, 1, 2, 3, 4). However, it is already the 6th in order LS-Level $3s3p^4$ ^4P formed by excitation 3*s*-electron, as a result, it is necessary to consider configurations with vacancies in the internal 3*s*-shell. The 8th in order also causes difficulties LS-Level $3s^23p^2$ (1D) $4s$ ^2D formed with an intermediate ^1D-, not ^3P-therm, as in other cases. All this requires significant adjustments to the scheme for calculating the configuration states of the phosphorus atom. Presence in the lower part of the spectrum of states with thawed 3*s*-shell indicates the need to take into account not only the valence, but also the core-valence correlation in calculations. A relatively small core charge and no strong splitting of levels on *LSJ*-sublevels indicates a relatively insignificant role of relativistic effects in calculating the lower energy levels of the *P* atom.

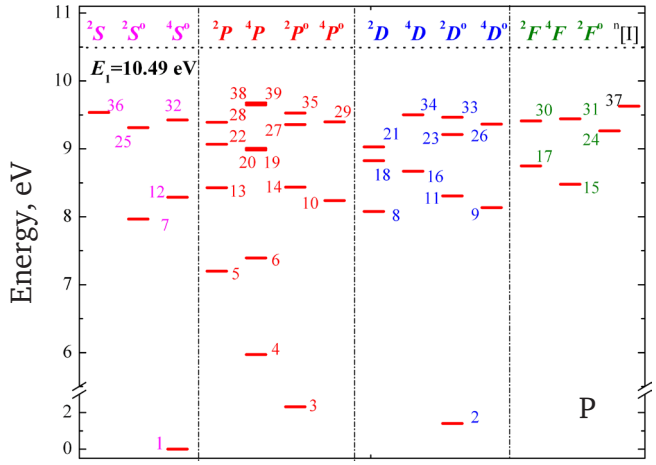

Figure 1. Layout of the 39 lower energy levels (in the LS representation) of the phosphorus atom (P I) and their distribution by terms according to NIST data

Table 1 shows the results of calculating the energies of 36 lower levels of the *P* atom. The main attention is paid to obtaining the exact excitation energies of spectroscopic states under the first ionization threshold and taking into account the interelectronic correlation when calculating the corresponding wave functions. To control the accuracy of calculating the wave functions of the *P* atom, the oscillator forces between the main one – and two-electron junctions are also calculated. A comparison of multi-configuration Hartree-Fock (MCHF) excitation energies previously calculated by us with the NIST reference data [12].

Table 1. Excitation energies (в eB) of the phosphorus atom: our MCHF calculations of excitation energies are compared with the NIST data [12]

No.	Configuration	Term	Eex NIST	Eex MCHF	ΔEex
1	$3s^23p^3$	$^4S^o$	0.0	0.0	0.0
2	$3s^23p^3$	$^2D^o$	1.410	1.426	-0.016
3	$3s^23p^3$	$^2P^o$	2.323	2.294	0.030
4	$3s^23p^2(^3P)4s$	^4P	5.971	6.249	-0.278
5	$3s^23p^2(^3P)4s$	^2P	7.200	7.178	0.023
6	$3s^23p^4$	^4P	7.395	6.540	0.855
7	$3s^23p^2(^3P)4p$	$^2S^o$	7.965	8.008	-0.043
8	$3s^23p^2(^1D)4s$	^2D	8.078	8.337	0.259
9	$3s^23p^2(^3P)4p$	$^4D^o$	8.136	8.146	-0.011
10	$3s^23p^2(^3P)4p$	$^4P^o$	8.239	8.198	0.041
11	$3s^23p^2(^3P)4p$	$^2D^o$	8.306	8.801	-0.495
12	$3s^23p^2(^3P)4p$	$^4S^o$	8.286	8.383	-0.096
13	$3s^23p^2(^3P)3d$	^2P	8.429	8.727	-0.298
14	$3s^23p^2(^3P)4p$	$^2P^o$	8.437	8.338	0.099
15	$3s23p2(^3P)3d$	^4F	8.478	8.557	-0.079
16	$3s^23p^2(^3P)3d$	^4D	8.671	8.669	0.002
17	$3s^23p^2(^3P)3d$	^2F	8.749	8.763	-0.015
18	$3s^3p^4$	^2D	8.825	9.68	-0.858
19	$3s^23p^2(^3P)5s$	^4P	9.008	9.015	-0.006
20	$s^23p^2(^3P)3d$	^4P	8.984	8.057	0.927

Table 1, Continued

No.	Configuration	Term	Eex NIST	Eex MCHF	ΔEex
21	$3s^23p^2(^3P)3d$	^2D	9.029	8.933	0.096
22	$3s^23p^2(^3P)5s$	^2P	9.069	8.980	0.089
23	$3s^23p^2(^1D)4p$	$^2D^o$	9.211	9.349	-0.138
24	$3s^23p^2(^1D)4p$	$^2F^o$	9.265	9.265	0.000
25	$3s^23p^2(^3P)5p$	$^2S^o$	9.312	9.242	0.069
26	$3s^23p^2(^3P)5p$	$^4D^o$	9.364	9.286	0.078
27	$3s^23p^2(^1D)4p$	$^2P^o$	9.358	9.547	-0.189
28	$3s^23p^2(^3P)4d$	^2P	9.393	9.439	0.046
29	$3s^23p^2(^3P)5p$	$^4P^o$	9.398	9.298	0.10
30	$3s^23p^2(^3P)4d$	^2F	9.411	9.464	-0.053
31	$3s^23p^2(^3P)4d$	^4F	9.443	9.404	0.040
32	$3s^23p^2(^3P)5p$	$^4S^o$	9.425	9.370	0.055
33	$3s^23p^2(^3P)5p$	$^2D^o$	9.464	9.378	0.086
34	$3s^23p^2(^3P)4d$	^4D	9.503	9.418	0.085
35	$3s^23p^2(^3P)5p$	$^2P^o$	9.527	9.273	0.253
36	$3s^23p^2(^1S)4s$	^2S	9.536	9.664	0.128

Table 1 shows that in the case of a phosphorus atom, the standard procedure for calculating the energies of spectroscopic states using orbitals that are orthogonalized in independent calculations for individual terms is very complicated. So, for example, for terms ^{4}P it is necessary to calculate single electron orbitals of configurations $3s^23p^2(^3P)4s$; $3s3p^4$; $3s^23p^2(^3P)5s$, $3d$, $4d$, $6s$ with two different atomic residues $3s^23p^2(^3P)$ and $3s3p^4$. This necessitates the consideration in further calculations of two different $3p$-orbitals of the atomic phosphorus residue for this term.

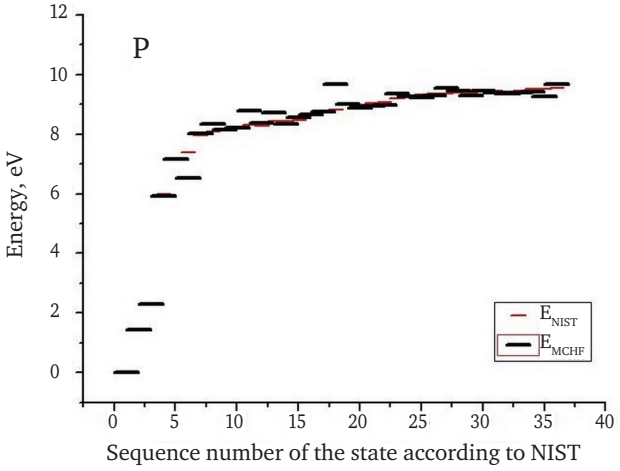

Figure 2. The layout of the energy thresholds of the excitation of the phosphorus atom. Date from our MCHF calculations (E_{MCHF}) compared with the NIST data (E_{NIST})

Figure 2 compares calculated by us MCHF-excitation energies of EMCHF with the NIST reference data (E_{NIST}). The accuracy of MCHF energies obtained in this case is mostly in the range of ~ 0.05-0.2 eV, which makes it possible to use them to calculate the processes of electron scattering on the *P* atom. As can be seen from Figure 2, the phosphorus atom is characterized by a fairly high ionization threshold E_{ion}=10.49 EV. However, there is too narrow an energy gap between the main $3p^3\,^4S^o$-state and lower excited states of the same configuration $3p^3\,^2D^o$ and $3p^3\,^2P^o$. In this case, the excitation energies of the above states are 0.0; 1.4097 and 2.3234 eV, respectively.

B) Energy Structure of the S Atom

Using the MCHF program code [2], we calculated 35 lower states of the *S* atom with configurations $1s^22s^22p^63s^23p^4$ (^3P,^1D, ^1S), $3s^23p^3$ ($^4S^o$) *nl* (n=3, 4, 5, 6; l = 0, 1, 2), $3s^23p^3$ ($^2D^o$) *nl* (n= 4; l= 0, 1), $3s^23p^3$ ($^2P^o$) 4*s* and $3s3p^5$($^{3,1}P^o$). As in the case of the phosphorus atom, the spectrum of the sulphur atom, according to NIST data [13], cannot be attributed to simple ones. As can be seen from Figure 2, the phosphorus atom is characterized by a fairly high ionization threshold E_{ion}=10.49 eV. The bottom three (^3P, ^1D, ^1S) levels correspond to the ground state configuration $3s^23p^4$ with energies of 0,02427, 1,1454 and 2,7500 EV, respectively. The value of the ground state energy is obtained by weight averaging the levels of the fine structure of the triplet $3s^23p^4$ $^3P_{0,1,2}$ when switching from *LSJ-NIST* image [13] to the approximation we used *LS*-coupling. The next few levels of the *P* spectrum are formed mainly by the excitation of one 3*p*-electron from the valence shell at one of the spectroscopic levels of configuration $3s^23p^3$ ($^4S^o$) *nl* (n= 3, 4, 5, 6, 7; l=0, 1, 2, 3, 4). However, already the 9th and 11th *LS*-levels $3s^23p^3$ (^2D) 4*s* ^{3,1}D formed with an intermediate ^{2}D-, not $^4S^o$ term. Even more difficult to calculate is the 15th *LS*-level $3s3p^5\,^3P^o$ with thawed 3*s*-shell. The presence in the lower part of the spectrum of the *S* atom of states with a thawed 3*s* shell indicates the need to consider not only valence but also core-valence correlation in the calculations. In addition, the presence of a stable negative sulphur ion S^- with configuration $3p^5$ $P_{3/2}$ and the affinity energy of 2,0771 eV indicates the need to take into account the valence and core-valence correlations in the calculations of processes of e+S-scattering.

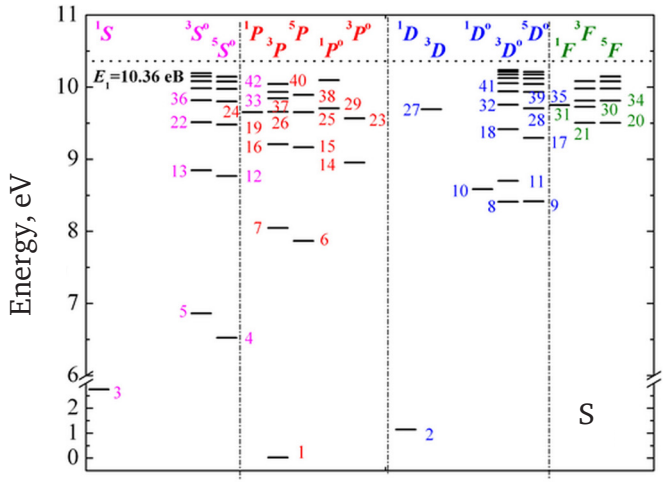

Figure 3. Layout of the 42 lower energy levels (in the LS representation) of the sulphur atom and their distribution by temperature according to NIST data [13]

Figure 4 shows a comparison of multiconfiguration Hartree-Fock (MCHF) excitation energies E_{MCHF} with NIST reference data [13] E_{NIST}. The accuracy of the obtained MCHF-excitation energies of the states of the *S* atom is ~ 0.04-0.2 eV. When calculating wave functions and excitation energies, the main attention is paid to taking into account the effects of valence and core-valence correlation. To control the accuracy of the calculated wave functions of an atom *S* the oscillator forces for single- and two-electron junctions are also calculated.

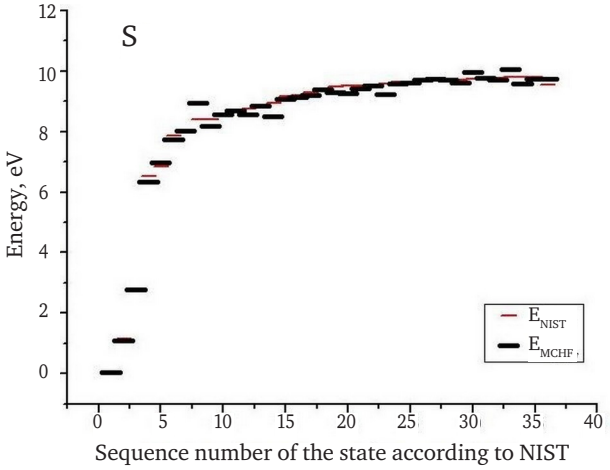

Figure 4. Layout of excitation energy thresholds Eexitof the sulphur atom. The results of our MCHF calculations are compared with NIST data [13]

The numerical values of the excitation energies obtained in MCHF calculations are presented in the Table 2. The results of our calculations are in good agreement with the data of the NIST database [13].

Table 1. Excitation energies (in EV) of the sulfur atom [12]

No.	Configuration	Term	Eex NIST	Eex MCHF	ΔEex
1	$3s^23p^4$	^3P	0,024	0,024	0,000
2	$3s^23p^4$	^1D	1,145	1,089	0,057
3	$3s^23p^4$	^1S	2,750	2,765	-0,015
4	$3s^23p^3(^4S^o)4s$	$^5S^o$	6,524	6,337	0,187
5	$3s^23p^3(^4S^o)4s$	$^3S^o$	6,860	6,974	-0,114
6	$3s^23p^3(^4S^o)4p$	^5P	7,868	7,744	0,124
7	$3s^23p^3(^4S^o)4p$	^3P	8,045	8,020	0,026
8	$3s^23p^3(^2D^o)4s$	$^3D^o$	8,410	8,940	-0,530
9	$3s^23p^3(^4S^o)3d$	$^5D^o$	8,417	8,171	0,246
10	$3s^23p^3(^2D^o)4s$	$^1D^o$	8,584	8,575	0,010
11	$3s^23p^3(^4S^o)3d$	$^3D^o$	8,700	8,705	-0,005
12	$3s^23p^3(^4S^o)5s$	$^5S^o$	8,766	8,569	0,197
13	$3s^23p^3(^4S^o)5s$	$^3S^o$	8,846	8,839	0,008
14	$3s3p^5$	$^3P^o$	8,952	8,508	0,444
15	$3s^23p^3(^4S^o)5p$	^5P	9,165	9,059	0,106
16	$3s^23p^3(^4S^o)5p$	^3P	9,208	9,131	0,077
17	$3s^23p^3(^4S^o)4d$	$^5D^o$	9,296	9,188	0,108
18	$3s^23p^3(^4S^o)4d$	$^3D^o$	9,417	9,393	0,024
19	$3s^23p^3(^4S^o)6s$	$^5S^o$	9,480	9,298	0,183
20	$3s^23p^3(^4S^o)4f$	^5F	9,504	9,276	0,228
21	$3s^23p^3(^4S^o)4f$	^3F	9,504	9,421	0,083
22	$3s^23p^3(^4S^o)6s$	$^3S^o$	9,512	9,514	-0,002
23	$3s^23p^3(^2P^o)4s$	$^3P^o$	9,567	9,222	0,345
24	$3s^23p^3(^4S^o)6p$	^5P	9,653	9,583	0,069
25	$3s^23p^3(^2D^o)4p$	^1P	9,653	9,627	0,026
26	$3s^23p^3(^4S^o)6p$	^3P	9,658	9,708	-0,049
27	$3s^23p^3(^2D^o)4p$	^3D	9,693	9,727	-0,034
28	$3s^23p^3(^4S^o)5d$	$^5D^o$	9,704	9,714	-0,010
29	$3s^23p^3(^2P^o)4s$	$^1P^o$	9,707	9,611	0,096
30	$3s^23p^3(^2D^o)4p$	^3F	9,725	9,970	-0,245
31	$3s^23p^3(^2D^o)4p$	^1F	9,750	9,770	-0,020
32	$3s^23p^3(^4S^o)5d$	$^3D^o$	9,757	9,704	0,052
33	$3s^23p^3(^4S^o)7s$	$^5S^o$	9,802	10,073	-0,271
34	$3s^23p^3(^4S^o)5f$	^5F	9,812	9,583	0,230
35	$3s23p3(^4S^o)5f$	^3F	9,813	9,726	0,086

Conclusions

Comparison of the excitation energies of *P* and *S* atoms calculated in the approximate LS-coupling with the available experimental data indicates the high efficiency and accuracy proposed in

BSR-versions of the method *R*-matrix based on the use of non-orthogonal orbitals and *B*-splines as basic functions. The accuracy achieved is ~ 0.05-0.2 eV for lower energy levels. The oscillator forces for the main one- and two-electron junctions in phosphorus and sulphur atoms are also calculated. The electronic wave functions calculated in the MCHF approximation fully take into account the effects of electronic correlations. The values of the excitation energies and wave functions of the 36 lowest states of the *P* atom and the 35 lowest states of the *S* atom calculated by us will be used in the future to calculate the complete and differential cross-sections of slow electron scattering on phosphorus and sulphur atoms.

References

[1] Zatsarinny O. B-spline atomic R-matrix codes. *Comput. Phys. Commun*. 2006;174(4):273-356.
[2] Froese Fischer C. The MCHF atomic-structure package. *Comput. Phys. Commun.* 1991;(64):369-98.
[3] Zatsarinny O, Bartschat K, Gedeon S, Gedeon V, Lazur V. Low-energy electron scattering from Ca atoms and photodetachment of Ca-. *Phys. Rev. A.* 2006;74(5):052708.
[4] Zatsarinny O, Bartschat K, Bandurina L, Gedeon S. Electron-impact excitation of calcium. *J. Phys. B.* 2007;40(20):4023-31.
[5] Zatsarinny O, Bartschat K, Gedeon S, Gedeon V, Lazur V, Nagy E. Cross sections for electron scattering from magnesium. *Phys. Rev. A.* 2009;79(5):052709.
[6] Nagy EA. The cross sections of electron-impact scattering on Sr. *Scientific Herald of Uzhhorod University. Series "Physics".* 2009;(25):148-53.
[7] Gedeon V, Gedeon S, Lazur V, Nagy E, Zatsarinny O, Bartschat K. Electron scattering from silicon. *Phys. Rev. A.* 2012;85(2):022711.
[8] Gedeon V, Gedeon S, Lazur V, Nagy E, Zatsarinny O, Bartschat K. B-spline R-matrix-with-pseudostates calculations for electron collisions with aluminum. *Phys. Rev. A.* 2015;92(5):052701.
[9] Gedeon V, Gedeon S, Lazur V, Nagy E, Zatsarinny O, Bartschat K. Low-energy outer-shell photodetachment of the negative ion of aluminum. *J. Phys. B.* 2018;51(3):035004.
[10] Bandurina LO, Gedeon SV. The differential cross sections of electron scattering on neutral boron. *Scientific Herald of Uzhhorod University. Series "Physics".* 2015;(37):49-56.
[11] Nagy EA, Gedeon VF, Gedeon SV, Lazur VYu. Electron-impact excitation of 51S – 51Po resonance transition in Sr atom. *Ukr. Phys. J.* 2018;63(1):11-24.
[12] NIST. NIST Atomic Spectra Database (ver. 5.3) [Internet]. 2009 [updated 2020 October 30; cited 2019 Feb. 10]. Available from: http://physics.nist.gov/asd.
[13] NIST. NIST Atomic Spectra Database (ver. 4.1.0) [Internet]. 2010 [updated 2020 November 30; cited 2019 Jun. 24]. Available from: https://physics.nist.gov/PhysRefData/ASD/Html/verhist.shtml.

Список використаної літератури

[1] Zatsarinny O. B-spline atomic R-matrix codes. *Comput. Phys. Commun.* 2006;174(4):273–356.
[2] Froese Fischer C. The MCHF atomic-structure package. *Comput. Phys. Commun.* 1991;(64):369–98.
[3] Zatsarinny O, Bartschat K, Gedeon S, Gedeon V, Lazur V. Low-energy electron scattering from Ca atoms and photodetachment of Ca-. *Phys. Rev. A.* 2006;74(5):052708.
[4] Zatsarinny O, Bartschat K, Bandurina L, Gedeon S. Electron-impact excitation of calcium. *J. Phys. B.* 2007;40(20):4023–31.
[5] Zatsarinny O, Bartschat K, Gedeon S, Gedeon V, Lazur V, Nagy E. Cross sections for electron scattering from magnesium. *Phys. Rev. A.* 2009;79(5):052709.

[6] Nagy EA. The cross sections of electron-impact scattering on Sr. *Scientific Herald of Uzhhorod University. Series "Physics"*. 2009;(25):148–53.
[7] Gedeon V, Gedeon S, Lazur V, Nagy E, Zatsarinny O, Bartschat K. Electron scattering from silicon. Phys. Rev. A. 2012;85(2):022711.
[8] Gedeon V, Gedeon S, Lazur V, Nagy E, Zatsarinny O, Bartschat K. B-spline R-matrix-with-pseudostates calculations for electron collisions with aluminum. *Phys. Rev. A.* 2015;92(5):052701.
[9] Gedeon V, Gedeon S, Lazur V, Nagy E, Zatsarinny O, Bartschat K. Low-energy outer-shell photo-detachment of the negative ion of aluminum. *J. Phys. B.* 2018;51(3):035004.
[10] Бандурина ЛО, Гедеон СВ. Диференціальні перерізи розсіяння електронів на атомі бору. *Науковий вісник Ужгородського університету. Серія «Фізика».* 2015;(37):49–56.
[11] Nagy EA, Gedeon VF, Gedeon SV, Lazur VYu. Electron-impact excitation of 51S – 51Po resonance transition in Sr atom. *Ukr. Phys. J.* 2018;63(1):11–24.
[12] NIST. NIST Atomic Spectra Database (ver. 5.3) [Internet]. 2009 [updated 2020 October 30; cited 2019 Feb. 10]. Available from: http://physics.nist.gov/asd.
[13] NIST. NIST Atomic Spectra Database (ver. 4.1.0) [Internet]. 2010 [updated 2020 November 30; cited 2019 Jun. 24]. Available from: https://physics.nist.gov/PhysRefData/ASD/Html/verhist.shtml.

Розрахунки енергетичної структури атомів *P*, *S* методом *R*-матриці з *B*-сплайнами

Н.Ю. Кондор, О.В. Єгіазарян, В.Ю. Лазур

Ужгородський національний університет
88000, вул. Волошина, 54, м. Ужгород, Україна

Анотація

Мета. Протягом останніх десятиліть фізика електронно-атомних (ЕА) зіткнень інтенсивно розвивалася. Це пояснюється як фундаментальною природою досліджуваних процесів, так і прикладними потребами. Це насамперед про розуміння на глибокому рівні поведінки субмікроскопічних, часто сильно корельованих, квантово-механічних багаточастинкових систем. Результатом цього розуміння є отримання великої кількості даних, необхідних для моделювання поведінки різних типів плазми та розрядів, а також для діагностики їх властивостей.

Методи. У статті представлено загальні принципи та ідею, що лежать в основі методу *B*-сплайнової *R*-матриці (БСР) з неортогональними орбіталями. Використання неортогональних одноелектронних орбіталей усуває ортогональні обмеження, що застосовуються у багатьох інших теоретичних підходах. Ці обмеження було запроваджено виключно для зручності розрахунків, а не з міркувань фізичної необхідності. Відхиляючи умови ортогональності, метод БСР значно покращує точність опису цілі. Відповідно, стає можливим подальший точний розрахунок процесів зіткнення.

Результати. Було розглянуто застосування методу БСР для розрахунку енергетичної структури атомів фосфору та сірки, що представляє значний практичний інтерес. Результати розрахунків демонструють хорошу згоду з наявними експериментальними даними.

Висновки. У роботі розраховано енергетичну структуру атома фосфору. Результати розрахунків демонструють хорошу згоду з наявними експериментальними даними. Надалі наші дані буде використано при вивченні розсіювання електронів на атомах фосфору та сірки

Ключові слова: атом фосфору, атом сірки, обчислення структури атомних систем, метод *R*-матриці з *B*-сплайнами, метод Хартрі-Фока, багатоелектронні бази, кореляційна взаємодія, одно- і багатоконфігураційне наближення

Расчеты энергетической структуры атомов *P, S* методом *R*-матрицы с *B*-сплайнами

Н.Ю. Кондор, О.В. Егиазарян, В.Ю. Лазур

Ужгородский национальный университет
88000, ул. Волошина, 54, г. Ужгород, Украина

Аннотация

Цель. В течение последних десятилетий физика электронно-атомных (ЕА) столкновений интенсивно развивалась. Это объясняется как фундаментальной природой исследуемых процессов, так и прикладными потребностями. Это прежде всего о понимании на глубоком уровне поведения субмикроскопических, часто сильно коррелированных, квантово-механических многочастичных систем. Результатом этого понимания является получение большого количества данных, необходимых для моделирования поведения различных типов плазмы и разрядов, а также для диагностики их свойств.

Методы. В статье представлены общие принципы и идею, которые лежат в основе метода B-сплайновой R-матрицы (БСР) с неортогональными орбиталями. Использование неортогональных одноэлектронных орбиталей устраняет ортогональные ограничения, применяемые во многих других теоретических подходах. Эти ограничения были введены исключительно для удобства расчетов, а не из соображений физической необходимости. Отклоняя условия ортогональности, метод БСР значительно улучшает точность описания цели. Соответственно, становится возможным дальнейший точный расчет процессов столкновения.

Результаты. Было рассмотрено применение метода БСР для расчета энергетической структуры атомов фосфора и серы, что представляет значительный практический интерес. Результаты расчетов показывают хорошее согласие с имеющимися экспериментальными данными.

Выводы. В работе рассчитано энергетическую структуру атома фосфора. Результаты расчетов показывают хорошее согласие с имеющимися экспериментальными данными. В дальнейшем наши данные будут использованы при изучении рассеяния электронов на атомах фосфора и серы

Ключевые слова: атом фосфора, атом серы, рассчет структуры атомных систем, метод R-матрицы с B-сплайнами, метод Хартри-Фока, многоелектронные базы, кореляционное взаимодействие, одно- и многоконфигурационное приближение

Scientific Herald of Uzhhorod University
Series “Physics”

Journal homepage: https://physics.uz.ua/en
Issue 48, 78-91
Received: 02.08.2020. Revised: 05.10.2020. Accepted: 29.11.2020

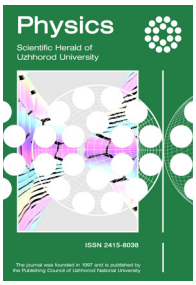

УДК 524.386
PACS 97.80.Hn
DOI: 10.24144/2415-8038.2020.48.78-91

Influence of Starspots and Pulsations on Determination of Third Body Orbital Parameters in Eclipsing Binary Systems

V.I. Kudak[1*], V.M. Perig[1], I.E. Molotov[2]

[1]Laboratory of space researches
Uzhhorod National University
88000, 2A Daleka Str., Uzhhorod, Ukraine

[2]Keldysh Institute of Applied Mathematics
Russian Academy of Sciences
125047, 4 Miusskaya Sq., Moscow, Russia

Abstract

Purpose. Defined the influence of starspots and pulsation of eclipsing binary components on the possibility of the third body determination in eclipsing binary systems and estimation of orbital parameters errors caused by such factors.

Methods. In this paper method of O-C diagrams was used to detect the eclipsing binary system period change caused by the presence of the third body. Monte Carlo simulations were used to estimate values of third body orbital parameters that correspond to obtained O-C diagrams. This method is compiled in “OCFit” software.

Results. Different cases of starspots and pulsation are considered. The precision of orbital parameters calculated for these cases.

Conclusions. Detached EB systems with spot are not sophisticated objects for 3rd body detection. Contact EB systems with migrated spots are more complicated systems to search third bodies and detect their orbital parameters. In the case of EB system pulsation most precise results can be obtained with a long period of pulsations. Resolution of the light curve is very important to make good O-C diagram.

Keywords: variable stars, eclipsing binary systems, O-C diagram, starspots, pulsations

Suggested Citation:
Kudak VI, Perig VM, Molotov IE. Influence of starspots and pulsations on determination of third body orbital parameters in eclipsing binary systems. *Scientific Herald of Uzhhorod University. Series “Physics”*. 2020;(48):78-91.

*Corresponding author

Introduction

Eclipsing binary (EB) systems are objects of research in different aspects of astronomy, one of them is searching of third bodies in EB systems. For these purposes O-C diagram method is commonly used. In this paper, we will describe some factors that have an influence on the light curve minima shape of EB systems, and therefore on shape of O-C diagram too. Such factors are: presents of *spots* on EB component, or on both components and *pulsations* of EB system.

Our simulations are based on a light curves (LC) generated by PHOEBE software [1] based on well-known Wilson & Devinney code described in work [2]. These LC will be extended for needed number of cycles, usually 5 or 10 years. Time shifts in LC caused by presence of 3rd body will be added based on computation made in work [3; 4]. On the final stage other distortion factors mentioned above are also added to LC. Orbital elements of 3rd body will be determined from O-C diagrams using Monte Carlo simulations by "OCFit" software described in [5]. In our simulation we use EB stars that are located near the north pole to get maximum data coverage.

Spots in EB Systems

In this section we will try to simulate O-C diagrams in ideal terrestrial conditions but under the influence of other non-terrestrial factors like star-spots. As we know the formation of starspots depends on the age of a host star, that's why we should separate our simulation for detached and contact EB systems. But before we start to simulate we need to know some general spot parameters for this EB systems. Its a radius of star spot, its temperature, and life cycle. Do the spot disappear after some short time or can be present on a host star for a relatively long time like 5-10 years? The spots migrate or not?

In work [6] authors have shown that intensity variations resulting from star-spots (not taking into account Wilson depressions) can introduce disturbances of up to ~ 0.01 day in the O-C residuals of contact binaries. Given the rapid evolutionary time-scales of spots (of the order of days) seen in recent Doppler images of the contact binary AE Phe [7] this may lead to explaining some of the observed jitter in the O-C curves of these objects. But in work [8], the effects of a Wilson depression seem to result in a scatter of only a few seconds in the O-C residuals, it seems unlikely that the Wilson depression will be a significant source of jitter for contact binaries. Such changes resulting from star-spots would be distinguishable from other mechanisms that cause period changes and it should still be possible to determine the orbital period accurately [8].

Several studies have indicated that spot on close binaries can have angular diameters from 10° to 40° which means that they will cover from 5 to 25% of the whole photosphere of the active components (e.g. [9; 10]). In most cases, active component can have one or two giant spots. It is also argued that such spots can remain on a surface from a few years to even ten years [6]. For a estimation of maximum effect caused by the star spot, it is assumed that in our simulations spots are located on equator of each component. According to [6] spots with angular diameter less then 10° cause negligible shifts of the light minimum of the primary eclipse. Therefore we will not consider with spots smaller then 10° (Fig. 1).

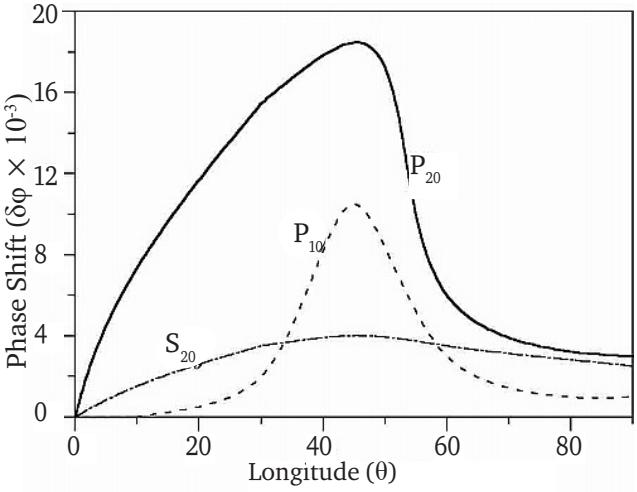

Figure 1. Phase shift δφ(θ) of the primary eclipse of a contact binary similar to AB And. Curves labelled by "P" correspond to a spot on the primary, while "S" refers to a spot on the secondary component [6]

Furthermore, the spots on secondary component always remain visible during the primary eclipse, while the spots on primary do not. As a result, the spots on primary cause a significantly greater photometric perturbation to the light curve than the spots on secondary component. In paper [6] authors also showed that unlike real orbital period changes, non-migrating star spots cannot cause permanent slopes in the O-C diagrams. But the O-C differences caused by long-lived migrating spots can be expected to be periodic.

Detached EB Systems

Tidal interactions force most of these stars to rotate synchronously with their orbital motions. The rapid rotation combined with deep convection envelopes produces a variety of magnetic activity phenomena including starspots in these stars. Brightness variations due to starspots can be observed in detached EB only during primary total eclipses when the luminous hot components are hidden. Therefore, because of synchronized rotation, only one hemisphere of the cool stars can be observed and the photometric data collected are less detailed than for other spotted binaries [11].

For detached eclipsing binary systems spots with radius from 5° to 25° are usually typical, we can find such systems in many publications like e.g. [12] or in publications about spots in RSCVn binaries systems (e.g. [13-15]). Objects with spots migrations are very rarely observed, so we will not consider such a case. Model of detached EB system is presented on Figure 2, the main parameters of this system are listed in the Table 1.

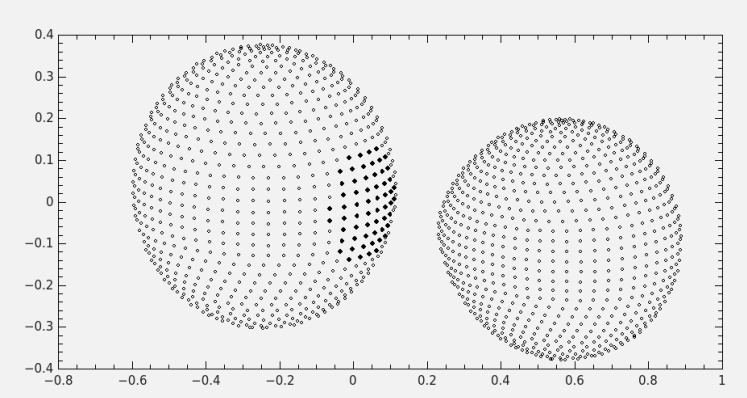

Figure 2. Model of detached EB system with spot (colat=90°, colon=0°) in plane of sky view at phase 0.15

Table 1. Basic parameters of detached binary system presented on Figure 2. HJD0 is a origin of the ephemeris; P – orbital period of EB system; SMA – semi-major axis; RM – mass ratio; VGA – centre of mass velocity, INCL – inclination

HJD0(day) P(day)	2451852,3783 1,42834
SMA ($R_\odot$) RM	1,000 0,432
VGA (km/s)	0
INCL (°)	77,690

As we mentioned above, spots with a radius less then 10° do not have a big influence on O-C diagram. So, we will consider how starspot located on stars equator (colat=90°, lon=0°) with radius r_{spot}=15° and r_{spot}=25° affect the O-C diagram. There is also a difference in a hot and cold

spot. The hot spot will have T_{spot}=1.2, where T_{spot} is the ratio between the temperature of the spot and the local temperature of the underlying photosphere, the cold spot will be defined as T_{spot}=0.8. On Figure 3 we can see how hot and cold spots affect the shape of the minima. Mainly primary minima are changing their shape under the influence of spots.

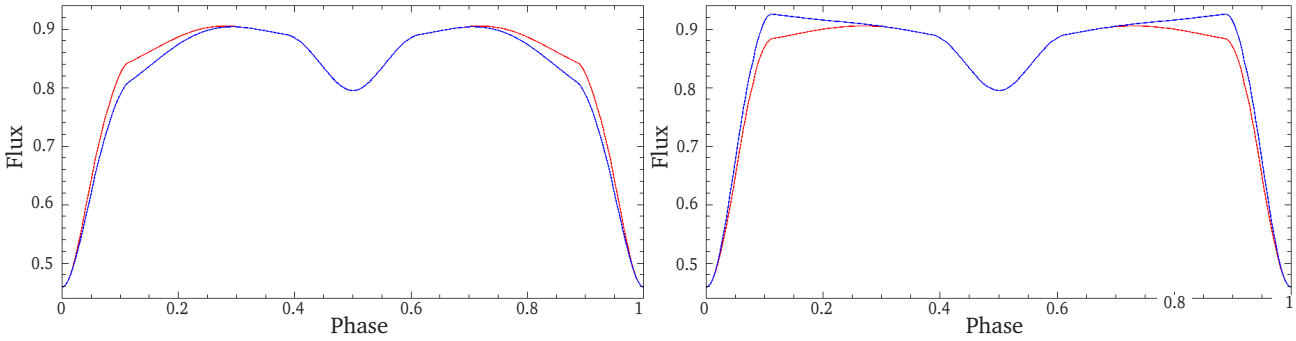

Figure 3. Spot on primary component with different temperature and radius. Blue line – spot radius 25°, red line – spot radius 15°

The final O-C diagrams for all four cases are presented in Figure 4. Looking only on O-C diagram we can't clearly see the difference. Only when we fit these O-C diagrams by MCMC method results are getting clearer. Final solutions of fitting are presented in Table 2.

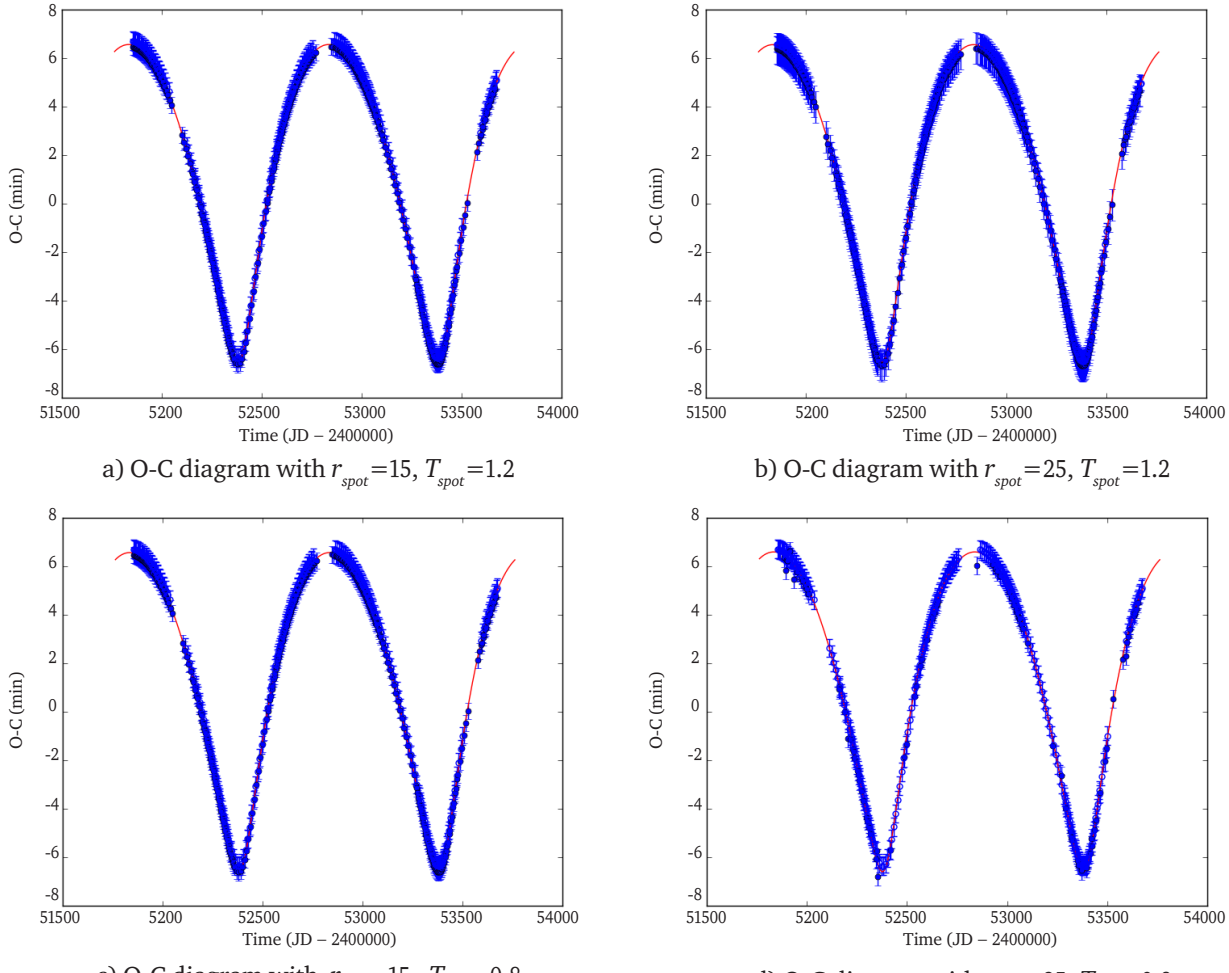

a) O-C diagram with r_{spot}=15, T_{spot}=1.2

b) O-C diagram with r_{spot}=25, T_{spot}=1.2

c) O-C diagram with r_{spot}=15, T_{spot}=0.8

d) O-C diagram with r_{spot}=25, T_{spot}=0.8

Figure 4. O-C diagram for EB system with different r_{spot} and T_{spot}. Red line – fit with MCMC method, correspond to values in Table 2. Filled circles are primary minima, not filled circles – secondary minima

Analysing χ^2 value of 4 cases we can state that case of spot with parameters T_{spot}=1.2 and r_{spot}=25° is fitted the best. The precision of fit depends on the accuracy of minima determination that can vary depending on the method we used. In case of a spot with parameters T_{spot}=1.2 and r_{spot}=25° precision of minima determination was almost the same for primary and secondary minima.

Table 2. Orbital parameters of 3rd body for detached EB system with different spot parameters rspot and T_{spot}. P – orbital period of eclipsing pair, T_0 – initial minimum, P_3 – orbital period of the 3rd body, t_{03} – pericenter passage, a sin i_3 – projected semi-major axis of the orbit, e_3 – eccentricity, ω_3 – the longitude of the periastron, $f(M_3)$ – the mass function, χ^2 – sum of squares of the best fit, χ^2/n – reduced sum of squares (n – number of data points), errors are given in parenthesis

Solution	Original	r_{spot}=25 T_{spot}=1.2	r_{spot}=25 T_{spot}=0.8	r_{spot}=15 T_{spot}=1.2	r_{spot}=15 T_{spot}=0.8
P [days]	1,42834	fixed	fixed	fixed	fixed
T_0 [HJD]	2451852,3783	fixed	fixed	fixed	fixed
P_3 [days]	1000	1000(1)	1000,0(7)	1000(1)	1000,8(9)
t_{03} [HJD]	2451400	2451397(3)	2451397(1)	2451396(2)	2451396(2)
a sin i_3 [AU]	0.797	0.801(2)	0.803(3)	0.806(4)	0.802(3)
e_3	0.54	0.552(3)	0.559(4)	0.572(5)	0.563(3)
ω_3[°]	288	287,2(8)	287,1(6)	286,9(8)	286,9(7)
$f(M_3)$ [$M_\odot$]	–	0,0685(7)	0.0690(7)	0.0697(10)	0.0691(7)
χ^2	–	7,326	35,990	30,227	39,209
χ^2/n	–	0.0127	0.0654	0.0767	0.0993

It was mentioned above that spot on secondary component do not have a big influence on minima shape, so we will not consider here this option. As a conclusion we can say that detached EB systems with spot are not sophisticated objects for 3rd body detection. In case of bigger then 25° spots on the surface it is advisable to cut off from the top the height of primary (or secondary) minima to get better fit and to determine the time of minima more precisely.

Contact EB Systems

Contact binary stars occur relatively often among binaries (95% of eclipsing binary variables in the solar neighbourhood) [16]. A contact binary system consists of two dwarf stars, most often from the F, G, and K spectral classes, that are surrounded by a common convective envelope. The orbital period distribution peaks in the 8 to 12 hour range. Most systems, though not all, have orbital periods between 0.2 and 1.0 days [17; 18]. While the masses of the two component stars of a contact binary are typically unequal, the two stars usually have approximately equal surface temperatures due to the effects of mass and energy transfer between the components via a common convective envelope [19]. Eclipsing contact binaries are often referred to as W UMa systems in honor of the prototype [20].

The components of such a contact binary rotate very rapidly in spite of their old ages (v sin i ~ 100-200 km s^{-1}) as a result of spin-orbit synchronisation due to strong tidal interactions between the stars [11]. Many contact binaries show signs of stellar activity, presumably because the component stars are rapid rotators with deep convective zones. A study of the contact binaries with Doppler imaging technique reveals that both

components can be covered by cool starspots, with a tendency for the primary to be more active than the secondary [7; 21; 22].

This makes contact binaries excellent laboratories in which to investigate the temporal variations and evolution of stellar spots, in part because the timescales of the variations are shorter than in other types of binary and single stars. However, the shortest among these timescales can be problematic to study using groundbased observatories because they are comparable to the length of an Earth night. In [6] authors noted that the migration of starspots on the surface(s) of the constituent stars in short-period binaries, especially contact binaries, could affect measurements of eclipse times and thereby mimic changes in the orbital period [20]. Model of contact EB system with spot is presented on Figure 5, orbital parameters can be found in Table 3.

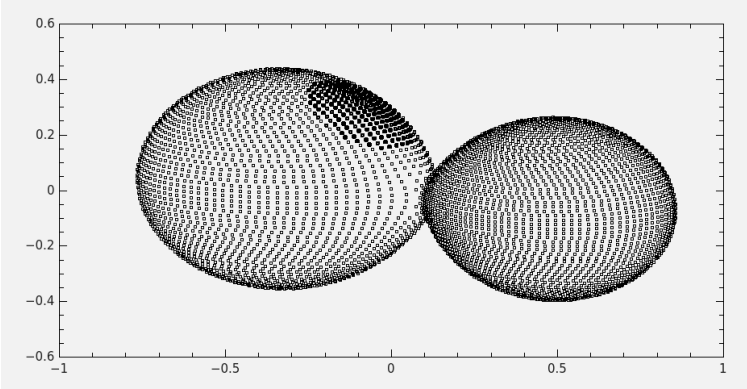

Figure 5. Model of contact EB system with spot (colat=45°, colon=0°) in plane of sky view at phase 0.15

Table 3. Baisic parameters of contact binary system presented on Figure 5. HJD0 is a origin of the ephemeris; P – orbital period of EB system; SMA – semi-major axis; RM – mass ratio; VGA – centre of mass velocity, INCL – inclination

HJD0(day) P(day)	2451852,3783 1,42834
SMA ($R_{\odot}$) RM	1.76 0.67
VGA (km/s)	4.70
INCL (°)	79.50

Light curve from such EB system will be subjected to changes depending on the position of the spot, such changes are partially presented on Figure 6, 7. Analyzing these data we can conclude that the most noticeable changes in LC are caused by changes of position in longitude of a starspot on the primary component of contact binary EB system. If we change spot position only in colatitude and leave longitude equal to 0°, we will observe only variation of primary minima shape and depth. On the other hand if we make colatitude constant (colatitude=45°, Figs. 6, 7) and change longitude of spot then in addition to the primary minimum part of the LC between two minima will vary too. As it can be expected "hot" spot has a greater contribution to changes in LC than "cold" spot (Fig. 6b vs 7b).

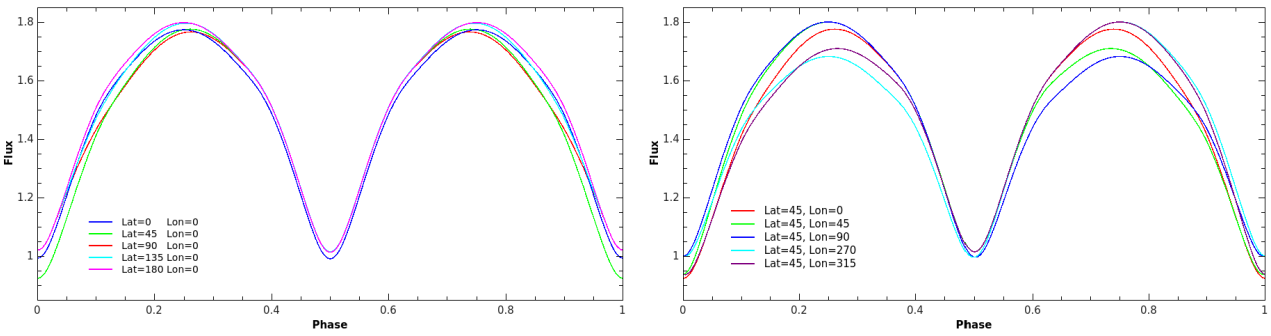

a) LC with spot on different colatitude and longitude=0°

b) LC with spot on different longitude and colatitude=45°

Figure 6. LC of contact binary system with "cold" spot (T_{spot}=0.8 T_{surf}) on primary component at different positions

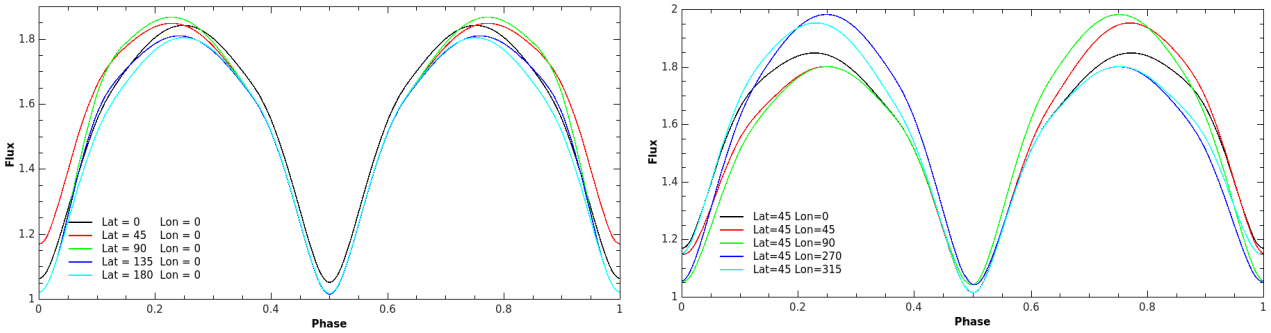

a) LC with spot on different colatitude and longitude=0°

b) LC with spot on different longitude and colatitude=45°

Figure 7. LC of contact binary system with "hot" spot (T_{spot} = 1.2 T_{surf}) on primary component at different positions

From previous results with detached EB system, we already know that smaller and colder spot adds more uncertainty to the definition of orbital elements of 3rd body available in EB system. We can expect the same results with contact EB systems. So let us define an influence of the spot presence on primary and secondary EB components and spot migration. This two aspects can be often found in contact and overcontact systems.

For simulation of O-C diagram with two spots in EB system we locate the spot on secondary component at lon=180°, $colat$=45° to make it visible to the observer. Radius of the spot on secondary component is r_{spot})=35°, temperature is T_{spot}=0.8 T_{surf}. The results of orbital parameters of 3rd body determination for this case are presented in third column of Table 4.

Table 4.Orbital parameters of 3rd body for contact EB system with two spots and migrated spot. Spot parameters r_{spot}=35°, T_{spot}=0.8 T_{surf}. For description of parameters see Table 2

Solution	Original	No spot	Two spots	Migrated spot
P [days]	1,42834	fixed	fixed	fixed
T_0 [HJD]	2451852,3783	fixed	fixed	fixed
P_3 [days]	1000	999,7(8)	999(1)	1000(1)
t_{03} [HJD]	2451400	2451400(2)	2451402(2)	2451398(4)
$a \sin i_3$ [AU]	0.797	0.799(3)	0.799(3)	0.764(3)
e_3	0.54	0,541(4)	0.532(5)	0.541(2)
ω_3 [°]	288	288,1(7)	288,5(8)	287(1)
$f(M_3)$ [$M_\odot$]	–	0.0681(8)	0.0683(9)	0.0666(7)
χ^2	–	0.614	6,547	2478,629
χ^2/n	–	0.0283	0.0719	6,1200

For simulation of O-C diagram with migrated spot over primary component of EB system we should define a parameters of the spot migration. According to [6] rotation period of starspot differs from P_{eq} by (1):

$$\Delta P = P_{\lambda} - P_{eq} \quad (1)$$

where P_{eq} is the equatorial period of rotation (P_{eq}=P_0), and P_{λ} is a period of starspot rotation equal to (2):

$$P_{\lambda} = P_{eq} \cdot (1 - k \cdot \sin^2 \lambda)^{-1} \quad (2)$$

in equation (2) k is a coefficient of differential rotation. For close binaries observation have indicated a range between $k \approx 6 \times 10^{-4}$ and 0.18 with mean value $\overline{k}=3\times10^{-2}$ [9]. At the end of each orbital cycle, a starspot will shift in longitude by (3):

$$\delta\theta = 2\pi \frac{\Delta P}{P} \quad (3)$$

If we calculate this value for our EB system with period P= 1,42834 which has spot on latitude λ=45° and mean value of $\overline{k}=3\times10^{-2}$, we will get $\delta\theta$=5,4798° or $\delta\theta \sim 5.5°$. So spot with such parameters will do a full revolution in ~ 65.5 cycles or in our case this is equal to 93.5 days. To simplify the process of simulation we take an integer number of $\delta\theta$=6° in such case the spot will do a full revolution in 60 cycles or in 85.7 days.

Large spots causing prominent light curve minima apparently can survive for many years, despite differential rotation, and form centres of activity, or active longitudes [11]. Polar spots are found to have lifetimes of over a decade [23]. Our simulation of 3rd body is made on 5 years time interval so lets define that our spot lifetime is also 5 years. Last question that we need to know is a radius of a spot. Lets consider a case with a spot radius 35° because a bigger spots are more typical for this type of EB systems.

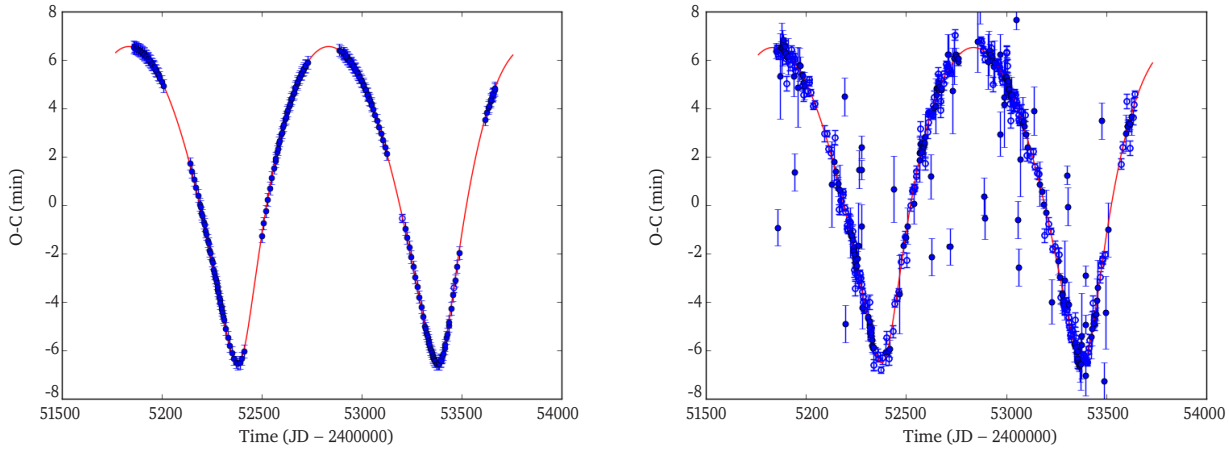

a) O-C diagram for ideal condition

b) O-C diagram for EB system with spot

Figure 8. O-C diagram for contact EB system with (b) and without (a) migrated spot. Red line – fit with MCMC method, correspond to values in Table 4. Filled circles are primary minima, not filled circles – secondary minima

From Figure 8 we can clearly see how migrated spot reduce precisions of minima exact time detection and in some cases, we even got point that does not fit in our O-C diagram. This means that these points are faults. Migrated spots are the most difficult cases for precise definition time of minima, make O-C diagram and define orbital parameters of 3rd body. Fitted parameters of orbit and χ^2 values of fit are presented in Table 4.

Pulsations in EB System

Pulsation in eclipsing binary systems can be observed in Algol-type binaries, the so-called oEA stars (oscillating EA stars). The oEA stars are mass-accreting main sequence A/F-type components in semidetached Algol-type eclipsing binary systems showing δ Sct – like pulsation [24]. The period of pulsation in such systems can vary from 20 to 300 minutes (see e.g [25; 26]).

In work [25] relation for period of pulsation

is given as (4):

$$P_{pul} = 0.031(4) + 0.009(1)P_{orb} \qquad (4)$$

This relation is based on observation of δ Sct stars in all known close binaries systems (Detached, Semi-detached, unclassified). Coefficient of correlation for this relation is r=0.62. To determine how the pulsations affect the O-C diagram and 3rd precision of orbital elements we will consider three cases of detached EB systems with a different period of pulsations: 30, 150, 300 minutes.

To define the precise time of minima with pulsation presence it is very important to have a high rate of observation per some time interval (or per LC). Until now we use synthetic LC generated by PHOEBE with sample rate 300 points per period. That was fully enough to precisely determine the time of the minima, but such rate is not enough for pulsations study.

To determine what sample rate should we use, let us check how the precision of primary minima is changed in detached EB system with added pulsations with parameters – period P_{pus}=30 min and amplitude A_{puls}=0.02. Three examples of same minima fitted in sample rates 300, 600 and 900 points per LC are presented on Figure 9.

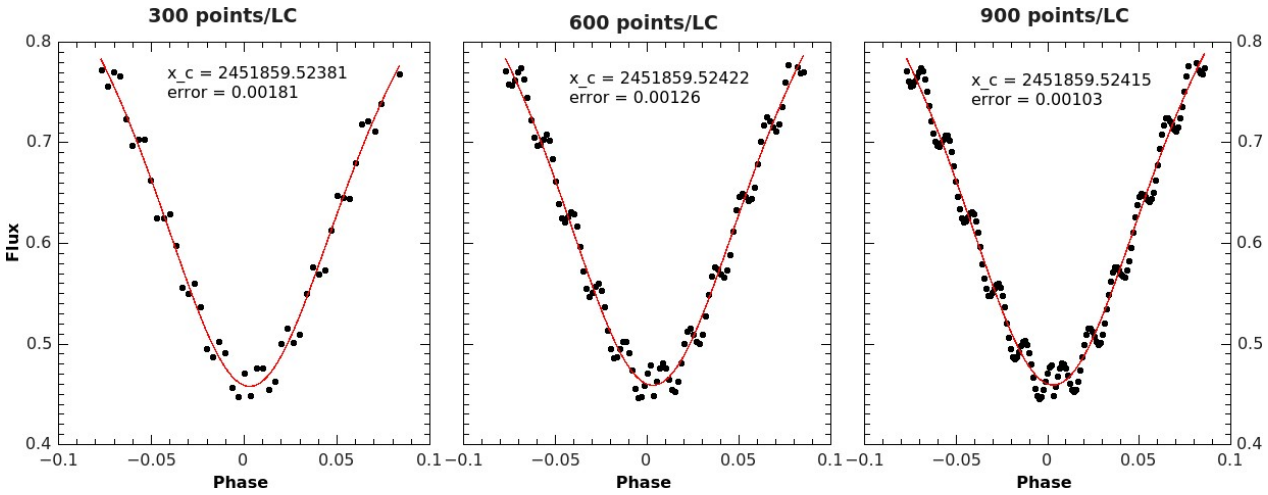

Figure 9. Different sample rate and precision of primary minima determination. Black point are data from LC, red line – fitted minima

If we have more than 900 points per LC then the precision of minima determination is slightly increasing to value 0.001 of a day. With the increase of sample rate, time of calculation also greatly increases, therefore the value of 900 points per LC is the best choice.

Third body orbit parameters determined in detached EB system with pulsation with a period of 30, 150 and 300 minutes are presented in Table 5.

Table 4.Orbital parameters of 3rd body for detached EB system with pulsations. For description of parameters see Table 2

Solution	Original	Pulsations P_{puls}=30 min	Pulsations P_{puls}=150 min	Pulsations P_{puls} = 300 min
P [days]	1,42834	fixed	fixed	fixed
T_0 [HJD]	2451852,3783	fixed	fixed	fixed
P_3 [days]	1000	1000(7)	1002(8)	1000(7)
t_{03} [HJD]	2451400	2451408(16)	2451390(19)	2451399(19)
$a \sin i_3$ [AU]	0,797	0,778(19)	0,813(19)	0,807(19)
e_3	0.54	0,431(29)	0,600(28)	0,569(30)
ω_3 [°]	288	291(5)	285(5)	288(5)
$f(M_3)$ [$M_\odot$]	–	0,0628(47)	0,0715(52)	0,0700(52)
χ^2	–	8,519	2,778	0,802
χ^2/n	–	0,0184	0,0069	0,0019

As we can see from a table, the most precise determination of orbit parameters corresponds to pulsation with the longest period. Vice versa most inaccurate parameters of orbit determination correspond to the shortest period. A short period of pulsations can't make it impossible to determine the precise time of minima, and as we show above it is also very important what resolution of LC do we have.

Conclusion

We made a review of starspots and pulsation influence on determination of 3rd body orbital parameters. In case of starpsot presence on the surface of EB system components we separate our simulation for detached and contact binary systems. First case is not so sophisticated systems for 3rd body detection, even when spot is available on the components of EB high precision of detected orbital elements can be achieved. For these case we also compare how hot and cold spots affect on the precision of 3rd body determination. As the result the hot spots have less influence on 3rd body orbit determination.

Second case with contact EB can represent more sophisticated examples of bigger starspots of EB components and several starspots at the time. This case more complicated and precision of orbital elements is reduces. Pulsation of EB systems is the most complicated case for 3rd body detection. In this situation is very important to achieve high sample rate to determine exact time of minima from light curve. As it can be seen from Table 5 biggest differences with original orbital elements of 3rd body are observed in case of short period pulsations. Such results are expected, but in this paper we made orbital elements accuracy analysis. Also larger samples studies are needed to statistically confirm our results.

References

[1] Prša A, Zwitter T. Computational guide to physics of eclipsing binaries. I. Demonstrations and perspectives. *Astrophys. J.* 2005;(628):426-38.
[2] Wilson RE, Devinney EJ. Realization of accurate close-binary light curves: Application to MR cygni. *Astrophys. J.* 1971;(166):605-19.
[3] Irwin JB. The determination of a light-time orbit. *Astrophys. J.* 1952;(116):211.
[4] Irwin JB. Standard light-time curves. *Astrophys. J.* 1959;(64):149-155.
[5] Gajdoš P, Parimucha Š. New tool with GUI for fitting OC diagrams. Proceedings of the 50th Conference on Variable Stars Research. 2018;(197):71-77.
[6] Kalimeris A, Rovithis-Livaniou H, Rovithis P. Starspots and photometric noise on observed minus calculated (O-C) diagrams. *Astron. Astrophys*. 2002;(387):969-76.
[7] Barnes JR, Lister TA, Hilditch RW, Collier Cameron A. High-resolution Doppler images of the spotted contact binary AE Phe. *Mon. Not. of the Royal Ast. Soc.* 2004;(348):1321-31.
[8] Watson CA, Dhillon VS. The effect of star-spots on eclipse timings of binary stars. *Mon. Notices Royal Astron. Soc.* 2004;351(1):110-116.
[9] Hall DS, Busby MR. Starspot lifetimes. In: Ibanoglu C, editor. Proceedings of the NATO Advanced Study Institute on Active Close Binaries; 1990 Sept. 11–22; Kusadasi. Turkey, September 11-22, 1989. Netherlands: Kluwer Academic Publishers; 1990. P. 377.
[10] Guinan EF, Giménez A. Magnetic activity in close binarie. Netherlands: Springer; 1993. The realm of interacting binary stars; pp. 51-110.
[11] Berdyugina SV. Starspots: A key to the stellar Dynamo. *Living Rev. Sol. Phys.* 2005;2(1):8.
[12] Liakos A, Zasche P, Niarchos P. A comprehensive study of six Algol type binaries. *New Astron.* 2011;16(8):530-38.
[13] Roettenbacher RM, Harmon RO, Vutisalchavakul N, Henry GW. A study of differential rotation on II Pegasi via photometric starspot imaging. *Astron. J.* 2011;141(4):138.

[14] Kővári Zs, Korhonen H, Kriskovics L, Vida K, Donati J-F, Le Coroller H, et al. Measuring differential rotation of the K-giant ζ Andromedae. *Astron. Astrophys.* 2012;(539):A50.
[15] Kozhevnikova AV, Alekseev IY. Long-term spottedness variations of 16 RS CVn stars. *Astron. Rep.* 2015;(59):937-51.
[16] Rucinski SM. Contact binaries of the galactic disk: Comparison of the baade's window and open cluster samples. *Astron. J.* 1998;116(6):2998-3017.
[17] Maceroni C, van't Veer, F. The properties of W Ursae Majoris contact binaries: New results and old problems. *Astron. Astrophys.* 1996;(331):523-31.
[18] Paczynski B, Szczygiel DM, Pilecki B, Pojmanski G. Eclipsing binaries in the all sky automated survey catalogue. *Mon. Not. of the Royal Ast. Soc.* 2006;(368):131-18.
[19] Lucy LB. The structure of contact binaries. *Astrophys. J.* 1968;(151):1123.
[20] Tran K, Levine A, Rappaport S, Borkovits T, Csizmadia Sz, Kalomeni B. The anticorrelated nature of the primary and secondary eclipse timing variations for the kepler contact binaries. *Astrophys. J.* 2013;(774):81.
[21] Maceroni C, Vilhu O, van't Veer F, van Hamme W. Surface imaging of late-type contact binaries I: AE Phoenicis and YY Eridani. *Astron. Astrophys.* 1994;(288):529-37.
[22] Hendry PD. Doppler imaging of VW cephei: Distribution and evolution of starspots on a contact binary. *Astrophys. J.* 2000;(531):467-93.
[23] Hussain GAJ. Starspot lifetimes. *Astron. Nachrichten.* 2002;(323):349-56.
[24] Rodríguez E, García JM, Costa V, Lampens P, van Cauteren P, Mkrtichian DE, et al. δ Sct-type pulsations in eclipsing binary systems: Y Cam. Mon. Not. of the Royal Ast. Soc. 2010;(408):2149-162.
[25] Liakos A, Niarchos P. Catalogue and properties of δ Scuti stars in binaries. *Mon. Not. of the Royal Ast. Soc.* 2017;(465):1181-200.
[26] Mkrtichian DE, Kim S-L, Rodriguez E, Olson EC, Nazarenko V, Gamarova AYu, et al. The oEA stars. *Solar and Stellar Physics Through Eclipses.* 2007;(370):194-200.

Список використаної літератури

[1] Prša A, Zwitter T. Computational guide to physics of eclipsing binaries. I. Demonstrations and perspectives. *Astrophys. J.* 2005;(628):426–38.
[2] Wilson RE, Devinney EJ. Realization of accurate close-binary light curves: Application to MR cygni. *Astrophys. J.* 1971;(166):605–19.
[3] Irwin JB. The determination of a light-time orbit. *Astrophys. J.* 1952;(116):211.
[4] Irwin JB. Standard light-time curves. *Astrophys. J.* 1959;(64):149–155.
[5] Gajdoš P, Parimucha Š. New tool with GUI for fitting OC diagrams. Proceedings of the 50th Conference on Variable Stars Research. 2018;(197):71–77.
[6] Kalimeris A, Rovithis-Livaniou H, Rovithis P. Starspots and photometric noise on observed minus calculated (O-C) diagrams. *Astron. Astrophys*. 2002;(387):969–76.
[7] Barnes JR, Lister TA, Hilditch RW, Collier Cameron A. High-resolution Doppler images of the spotted contact binary AE Phe. *Mon. Not. of the Royal Ast. Soc.* 2004;(348):1321–31.
[8] Watson CA, Dhillon VS. The effect of star-spots on eclipse timings of binary stars. *Mon. Notices Royal Astron. Soc.* 2004;351(1):110–116.

[9] Hall DS, Busby MR. Starspot lifetimes. In: Ibanoglu C, editor. Proceedings of the NATO Advanced Study Institute on Active Close Binaries; 1990 Sept. 11–22; Kusadasi. Turkey, September 11–22, 1989. Netherlands: Kluwer Academic Publishers; 1990. P. 377.
[10] Guinan EF, Giménez A. Magnetic activity in close binarie. Netherlands: Springer; 1993. The realm of interacting binary stars; pp. 51–110.
[11 Berdyugina SV. Starspots: A key to the stellar Dynamo. *Living Rev. Sol. Phys.* 2005;2(1):8.
[12] Liakos A, Zasche P, Niarchos P. A comprehensive study of six Algol type binaries. *New Astron.* 2011;16(8):530–38.
[13] Roettenbacher RM, Harmon RO, Vutisalchavakul N, Henry GW. A study of differential rotation on II Pegasi via photometric starspot imaging. *Astron. J.* 2011;141(4):138.
[14] Kővári Zs, Korhonen H, Kriskovics L, Vida K, Donati J-F, Le Coroller H, et al. Measuring differential rotation of the K-giant ζ Andromedae. *Astron. Astrophys.* 2012;(539):A50.
[15] Kozhevnikova AV, Alekseev IY. Long-term spottedness variations of 16 RS CVn stars. *Astron. Rep.* 2015;(59):937–51.
[16] Rucinski SM. Contact binaries of the galactic disk: Comparison of the baade's window and open cluster samples. *Astron. J.* 1998;116(6):2998–3017.
[17] Maceroni C, van't Veer, F. The properties of W Ursae Majoris contact binaries: New results and old problems. *Astron. Astrophys.* 1996;(331):523–31.
[18] Paczynski B, Szczygiel DM, Pilecki B, Pojmanski G. Eclipsing binaries in the all sky automated survey catalogue. *Mon. Not. of the Royal Ast. Soc.* 2006;(368):1311–18.
[19] Lucy LB. The structure of contact binaries. *Astrophys. J.* 1968;(151):1123.
[20] Tran K, Levine A, Rappaport S, Borkovits T, Csizmadia Sz, Kalomeni B. The anticorrelated nature of the primary and secondary eclipse timing variations for the kepler contact binaries. *Astrophys. J.* 2013;(774):81.
[21] Maceroni C, Vilhu O, van't Veer F, van Hamme W. Surface imaging of late-type contact binaries I: AE Phoenicis and YY Eridani. *Astron. Astrophys.* 1994;(288):529–37.
[22] Hendry PD. Doppler imaging of VW cephei: Distribution and evolution of starspots on a contact binary. *Astrophys. J.* 2000;(531):467–93.
[23] Hussain GAJ. Starspot lifetimes. *Astron. Nachrichten.* 2002;(323):349–56.
[24] Rodríguez E, García JM, Costa V, Lampens P, van Cauteren P, Mkrtichian DE, et al. δ Sct-type pulsations in eclipsing binary systems: Y Cam. Mon. Not. of the Royal Ast. Soc. 2010;(408):2149–162.
[25] Liakos A, Niarchos P. Catalogue and properties of δ Scuti stars in binaries. *Mon. Not. of the Royal Ast. Soc.* 2017;(465):1181–200.
[26] Mkrtichian DE, Kim S-L, Rodriguez E, Olson EC, Nazarenko V, Gamarova AYu, et al. The oEA stars. *Solar and Stellar Physics Through Eclipses.* 2007;(370):194–200.

Вплив плям та пульсацій на визначення елементів орбіти третього тіла в затемнювано подвійних системах

В.І. Кудак[1], В.М. Періг[1], І.Є. Молотов[2]

[1]Лабораторія космічних досліджень
Ужгородський національний університет
88000, вул. Далека, 2А, м. Ужгород, Україна

[2]Інститут прикладної математики ім. М.В. Келдиша
Російскої академії наук
125047, пл. Міуська, 4, м. Москва, Російська Федерація

Анотація

Мета. Визначено вплив зоряних плям та пульсацій компонентів затемнювано-подвійних систем на можливість виявлення третього тіла в цих системах та оцінку похибок орбітальних параметрів третього тіла викликаних такими чинниками.

Методи. У науковій роботі було використано метод O-C діаграм для виявлення зміни періоду затемнювано-подвійних систем, що викликані наявністю третього тіла в системі. Моделювання Монте-Карло були використані для оцінки значень орбітальних параметрів третього тіла, які відповідають отриманим O-C діаграмам. Цей метод закладено в програмне забезпечення «OCFit».

Результати. У дослідженні було розглянуто різні випадки зоряних плям та пульсацій. Було обчислено точність орбітальних параметрів третього тіла для цих випадків.

Висновки. Відокремлені затемнювано-подвійні системи з плямою не є складними об'єктами для виявлення 3-го тіла. Контактні затемнювано-подвійні системи з мігруючими плямами є більш складними випадками для пошуку третіх тіл та обчислення їх орбітальних параметрів. У випадку пульсацій затемнювано-подвійної системи найточніші параметри орбіти третього тіла можуть бути отримані при тривалому періоді пульсацій. Роздільна здатність кривої блиску є дуже важлива для створення хорошої O-C діаграми

Ключові слова: змінні зірки, затемнювано-подвійні системи, діаграма O-C, зоряні плями, пульсації

Влияние пятен и пульсаций на определение элементов орбиты третьего тела в затемнно двойных системах

В.И. Кудак[1], В.М. Периг[1], И.Е. Молотов[2]

[1]Лаборатория космических исследований
Ужгородский национальный университет
88000, ул. Далекая, 2А, г. Ужгород, Украина

[2]Институт прикладной математики им. М.В. Келдыша
Российской академии наук
125047, пл. Миусская, 4, г. Москва, Росийская Федирация

Аннотация

Цель. Определено влияние звездных пятен и пульсаций компонентов затменно-двойных систем на возможность обна- ружения третьего тела в этих системах и оценку погрешностей орбитальных параметров третьего тела вызванных такими факторами.

Методы. В научной работе использован метод О-С диаграмм для выявления изменения периода затменно-двойных систем, вызванных наличием третьего тела в системе. Моделирование Монте-Карло были использованы для оценки значений орбитальных параметров третьего тела, которые соответствуют получен-ным О-С диаграммам. Этот метод заложен в программное обеспечение «OCFit».

Результаты. БВ работе рассматриваются различные случаи звездных пятен и пульсаций. Точность орбитальных параметров третьего тела определена для этих случаев.

Выводы. Отделенные затменно-двойные системы с пятном не является сложными объектами для обнаружения 3-го тела. Контактные затменно-двойные системы с мигрирующими пятнами являются более сложным случаем для поиска третьих тел и вычисления их орбитальных параметров. В случае пульсаций затменно-двойной системы более точные параметры орбиты третьего тела могут быть получены при длительном периоде пульсаций. Разрешение кривой блеска очень важна для создания хорошей О-С диаграммы

Ключевые слова: переменные звезды, затменно-двойные системы, О-С диаграмма, звездные пятна, пульсации